Journal of Volcanology and Geothermal Research 469 (2026) 108496

Contents lists available at ScienceDirect

Journal of Volcanology and Geothermal Research

journal homepage: www.journals.elsevier.com/journal-of-volcanology-and-geothermal-research

Insights into the petrogenesis of alkalic, shonkinitic magmas from the Adel Hill Volcanic Field, Montana

C.L. McLeod [a,*], M.L. Lytle [a], T.J. Cracas [a], K.L. Brown [b], B.J. Shaulis [c], M. Loocke [d]

[a] Department of Geology and Environmental Earth Science, Miami University, 250 S. Patterson Avenue, Oxford, OH 45056, USA
[b] Department of Geology & Environmental Geoscience, DePauw University, 2 E Hanna St, IN 46135, USA
[c] Trace Element and Radiogenic Isotope Laboratory, University of Arkansas, Fayetteville, AR 72701, USA
[d] Department of Geology and Geophysics, Louisiana State University, Baton Rouge, LA 70803, USA

ARTICLE INFO

Keywords:
Shonkinite
Igneous petrology
Adel Hills
Alkali magmatism

ABSTRACT

Shonkinites are rare alkali-rich igneous rocks found in the geological record from the Precambrian to the Eocene. This study investigates the Upper Cretaceous shonkinites from the Adel Hills Volcanic Field (AHVF), central Montana. The AHVF shonkinites are porphyritic with large, euhedral to subhedral phenocrysts of diopside that exhibit sector zoning. Other major mineral phases include plagioclase, sanidine, and secondary zeolites. Minor and accessory phases identified with SEM-EDS include magnetite, apatite, rare ilmenite and pyrite, and secondary calcite. Bulk rock SiO_2 ranges from 47 to 49 wt% with $Na_2O + K_2O$ varying from 5.50 to 7.34 wt% within that silica range. Normalized bulk trace elements indicate LILE enrichment and Nb—Ta depletion, consistent with a volcanic arc setting. Bulk rock, diopside, and apatite chondrite-normalized REE signatures collectively exhibit a limited range of Eu anomalies (Eu/Eu* from 0.92 to 1.33). High-resolution elemental mapping of sector-zoned diopsides reveals that Si and Mg-enrichment is accompanied by Al, Ti, Na, and Cr-depletion within {−111} faces. In symmetrically equivalent prism sectors, Al, Ti, Na, and Cr enrichment with correlated depletions in Si and Mg is documented. This is interpreted to result from low degrees of undercooling during crystallization ($\Delta T = 13\text{-}25\ ^\circ C$). The lack of dendritic patterns at the Al sector boundaries further supports this. Apatite trace element chemistries are consistent with crystallization from mafic, alkali-rich melts while accompanying Ce/Ce* vs. Eu/Eu* systematics are consistent with formation in a hydrous, moderately oxidizing magmatic environment in which plagioclase crystallization was suppressed. Petrogenesis of the AHVF shonkinites is inferred to have occurred in a contractional tectonomagmatic setting in which variably metasomatized, heterogeneous mantle lithosphere experienced low degrees of partial melting. This occurred prior to the collapse of the Cordilleran fold and thrust belt and subsequent lithospheric extension in the middle Eocene-early Miocene.

1. Introduction

The study of igneous rocks has provided the foundation for our understanding of partial melting, magma generation, differentiation, crystallization, emplacement, and eruption, alongside the role these processes have played in Earth's physicochemical evolution over a range of spatial and temporal scales (e.g., Daly, 1914; Bowen, 1922, 1928; Holmes, 1932; Bowen, 1945; Tyrrell, 1978; Hanson, 1980; Wilson, 1989; Bowring and Housh, 1995; Shirey et al., 2008; Grove and Brown, 2018). From this, a tectonomagmatic framework has been established in which (broadly) characteristic textural, mineralogical, and geochemical signatures can be linked to specific tectonic environments, magmatic processes, and differentiation mechanisms (e.g., Jagoutz, 2014; Xia, 2014; Tang et al., 2019; Navarrete et al., 2020).

Recent advances in the understanding of magmatic processes have largely been achieved through the study of crystal cargoes and their associated crystal-scale features (e.g., compositional zoning, dissolution boundaries, reaction textures, overgrowths; Ohnenstetter and Brown, 1992; Mollo et al., 2010; Maruyama and Hiraga, 2017; Ubide et al., 2019; Zhou et al., 2021). Modern microanalytical techniques (e.g., scanning electron microscopy-energy dispersive spectroscopy, SEM-EDS; electron probe microanalysis, EPMA; and laser ablation inductively coupled plasma mass spectrometry, LA-ICP-MS) have made it possible to gain in-situ, spatially resolved chemical and physical

* Corresponding author.
E-mail address: mcleodcl@miamioh.edu (C.L. McLeod).

https://doi.org/10.1016/j.jvolgeores.2025.108496
Received 3 June 2025; Received in revised form 11 November 2025; Accepted 14 November 2025
Available online 20 November 2025

observations that have significantly improved our understanding of the chemical heterogeneity preserved within crystals at the millimeter to micron scale (Pollington and Baxter, 2011; Zhou et al., 2021; Kharkongor et al., 2023). For example, in clinopyroxenes, enrichments of Al and Ti and depletions of Si and Mg have been correlated with prism sectors and interpreted to reflect relatively low degrees of undercooling in a magmatic system, such as slow rates of magma ascent (Ubide et al., 2019; MacDonald et al., 2023, 2024; Simpson et al., 2025), while trace elements in apatite are increasingly used as petrogenetic indicators, with elemental abundances and ratios applied as tracers of melt origin and petrologic affinity (e.g., mafic vs. felsic, alkali-rich vs. metasomatic; O'Sullivan et al., 2020; Kieffer et al., 2023, 2024a, 2024b).

The majority of igneous rocks on Earth are subalkaline and include both tholeiitic and calc-alkaline series (e.g., Vermeesch and Pease, 2021). This subalkaline suite is characterized by saturation in silica with relatively low total alkalis (wt% $Na_2O + K_2O$) across the same range of wt% SiO_2 when compared to alkaline igneous rocks. Subalkaline igneous rocks are abundant throughout the magmatic rock record, from the extensive network of mid-ocean ridge basalts at divergent plate boundaries to the highly differentiated andesite to rhyolite suites at continental arcs, as well as within intraplate settings (e.g., Wilkinson, 1982; Burns and de Silva, 2023). In stark contrast, alkaline igneous rocks have relatively higher total alkali contents for the same range of silica exhibited by the subalkaline suite and represent <1 % of all igneous rocks on Earth. Despite their paucity, alkaline igneous rocks account for ~50 % of all igneous rock names and are associated with at least 400 alkaline rock types (Sørensen, 1974). The relatively high abundance of total alkalis, along with other highly incompatible elements (e.g., large ion lithophile elements; LILEs), at low silica contents in alkaline systems results in a relatively high abundance of minerals not typically found in subalkaline systems (e.g., nepheline, arfvedsonite, leucite). Their petrogenesis has, therefore, long fascinated geologists, not only from the perspective of mineral evolution but also for their potential to provide unique insights into petrogenetic processes that are otherwise not captured in subalkaline magmatic systems (e.g., Poletti et al., 2016; Wang et al., 2024).

Broadly, alkaline rocks form through low-degree partial melting of a range of potential sources, such as mafic lower crustal lithologies, metasomatized lithospheric mantle, the asthenospheric mantle, or enriched geochemical reservoirs deep within the mantle that have evolved due to variable inputs from ancient subduction systems over time (e.g., EMI, EMII; Chen et al., 2010; Poletti et al., 2016; Yaxley et al., 2022; Wang et al., 2024). They are found across various tectonic settings, from intraplate environments to volcanic arcs, to continental rift environments, and into post-orogenic continental regions (Nakamura et al., 1985; Philpotts and Ague, 2009; Cruz-Uribe et al., 2018; Wang et al., 2024). Historically, alkaline igneous systems have also been targeted for their mineral resources, as they often contain economically viable concentrations of rare-earth elements (REEs; e.g., Mountain Pass in California and Mt. Weld in Australia; USGS, 1952; Poletti et al., 2016; Cook et al., 2023; Chandler et al., 2024; Benson et al., 2025). Finally, the eruption of alkaline magmas has also been proposed as a potential mechanism for global warming due to the relatively higher abundance of dissolved CO_2 (which is released into the atmosphere during emplacement) compared to subalkaline systems (Foley and Fischer, 2017; Solomatova and Caracas, 2021; Wang et al., 2024).

This study investigates an alkaline igneous system to provide new crystal-scale insights into the magmatic processes related to the petrogenesis of alkali-rich magmas. Specifically, a suite of diopside-phyric shonkinite dikes are characterized for their textural, mineralogical, and geochemical signatures.

1.1. Shonkinites

Shonkinites were named after their type locality in the Shonkin Sag Laccolith in central Montana (Weed and Pirsson, 1895; Kendrick and Edmond, 1981; O'Brien et al., 1991; Ruggles et al., 2021). While the etymology of "Shonkin" is debated, it likely comes from the Blackfoot word "shonkan" meaning "to be brave/fearless" (Klassy, 2024). According to Weed and Pirsson (1895), the name of Shonkin Sag was derived from the Blackfeet Tribe's name for the nearby Highwood Mountains.

According to the International Union of Geological Sciences (IUGS), a shonkinite is defined as a plutonic rock where the modal proportion of feldspathoids (F) range from 10 % to 60 %, the ratio of plagioclase feldspar to the total amount of alkali feldspar and plagioclase (P/(A + P)) is ≤10, and the proportion of mafic minerals (M) is between 60 % and 90 %. The American Geosciences Institute describes a shonkinite as "a dark-colored syenite composed chiefly of augite and alkali feldspar, and possibly containing olivine, hornblende, biotite, and nepheline" (Neuendorf et al., 2005). Although these definitions aid in identifying shonkinites, they do not cover the mineralogical variations observed in shonkinitic rocks described in the literature (e.g., Beall, 1973; Shadenkov et al., 1990; Cunningham, 1999; Petrovskii et al., 2014; He et al., 2015; Poletti et al., 2016; Ghodke et al., 2018; Okrugin et al., 2018). Fig. 1 summarizes the global distribution of shonkinites as reported in the existing literature. Broadly, shonkinites range from porphyritic to phaneritic and feature a major mineral assemblage that includes clinopyroxene (typically diopside or augite), K-feldspar (usually sanidine and/or orthoclase), plagioclase, ± biotite, ± olivine, ± feldspathoids (typically nepheline), and ± amphiboles. See Table S1. Minor and accessory minerals consist of apatite, titanite, rutile, magnetite, spinel, barite, zeolite, calcite, and quartz, depending on the occurrence.

This study presents results from the first comprehensive petrographic and geochemical investigation of the mapped diopside-bearing shonkinite dikes in the Adel Hills Volcanic Field (AHVF) in north-central Montana. These intrusive features are ~70 miles west-southwest of the Shonkin Sag.

2. Geological setting

2.1. The Adel Hills Volcanic Field (AHVF)

The AHVF represents a spatially extensive, alkali-rich magmatic system. It is located within the Great Falls Tectonic Zone (GFTZ) and at the eastern terminus of the Montana Disturbed Belt (MDB; Fig. 2). It exists to the north of the Laramide Belt and the Helena Salient (Parker and Pearson, 2023). Previous work has proposed that the GFTZ represents either an intracontinental shear zone (e.g., Boerner et al., 1998) or a Paleoproterozoic suture between the older, Archean-aged, Hearne and Wyoming provinces which formed (in part) during ocean basin closure at ~1.9 Ga (Mueller et al., 2002). Generally, the MDB represents a northwest trending zone characterized by west-dipping thrust faults, which are post-dated by normal faults associated with Basin and Range lithospheric extension (Mudge, 1970). The AHVF is located northwest of the Helena Salient, an arcuate curve in the MDB (e.g., Harlan et al., 2008; Whisner et al., 2014; Howlett et al., 2024). Located near the Western Interior Seaway during the Late Cretaceous (see below), the AHVF formed within the retroarc foreland basin of the fold and thrust belt (Kauffman and Caldwell, 1993; Fuentes et al., 2012). The bedrock geology of the AHVF region is summarized in Fig. 2b and in the accompanying cross-section (after Vuke, 2000, 2014).

The AHVF is bound to the west by the Coburn Mountain thrust fault (Harlan et al., 2005) and unconformably overlies the Upper Cretaceous Two Medicine Formation. Proterozoic Belt Supergroup lithologies outcrop to the southwest with faulted (and repeated) mid-Paleozoic (Mississippian) to upper Mesozoic stratigraphy underlying and surrounding the AHVF (see cross-section, Fig. 2b). The observation of folding and imbricate thrust faulting of volcanic rocks in the southwestern region of the AHVF, the eastward thrusting of the Two Medicine Formation over AHVF units (see cross-section, Fig. 2b), and the overlapping of AHVF volcanic rocks (undeformed) onto Cretaceous strata in

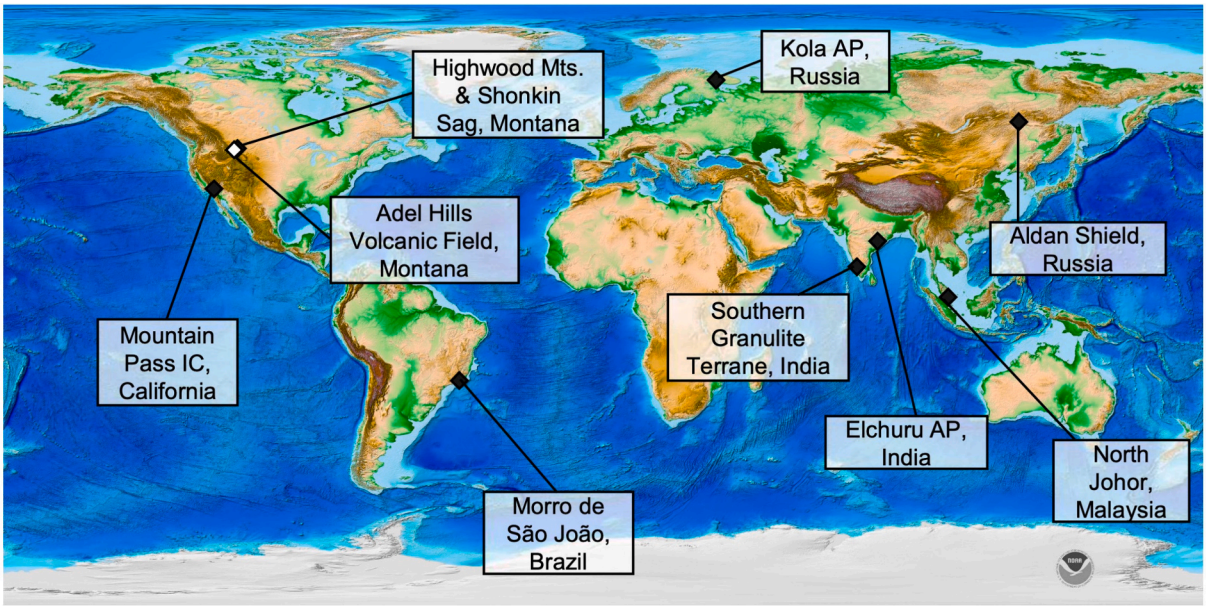

Fig. 1. Map of shonkinite localities discussed in the text. White diamond indicates the locale for this study, the Adel Hills Volcanic Field, Montana. AP = Alkaline Province, IC = Intrusive Complex. Base map from NOAA https://www.ncei.noaa.gov/products/etopo-global-relief-model. Locations sourced from Lyons (1944); Grubb (1965); Kendrick and Edmond (1981); O'Brien et al. (1991); Shadenkov et al. (1990); Madhavan et al. (1992); Saravanan and Ramasamy (1995); Brotzu et al. (2007); Rokosova and Panina (2013); Petrovskii et al. (2014); Bogatikov et al. (1994); Poletti et al. (2016); Rokosova et al. (2016); Okrugin et al. (2018).

the southeast implies that magmatic activity was syntectonic with respect to the thin skinned deformation of the MDB (Schmidt, 1978; Harlan et al., 2005).

The AHVF is characterized by lava flows, volcaniclastics (including ash-bearing breccias and conglomerates), dikes, and sills (see Fig. 3a; Lyons, 1944; Schmidt, 1978; Harlan et al., 2005). Present-day exposure of the AHVF (and associated intrusions) spans 900 km^2. In some areas, intercalated units of basaltic-andesite lavas, breccias, and other volcaniclastic units related to the eruption of a stratovolcano reach up to 1000 m in thickness (Lyons, 1944; Harlan et al., 2005; Scarberry et al., 2020). Early geochronologic work by Bellon et al. (1989) reported K—Ar ages from the AHVF ranging from 74.2 to 60.4 Ma, but as was later noted, the field sampling locations and sample descriptions were poorly documented (Harlan et al., 2005). Similar attempts to constrain the timing of AHVF magmatic activity were detailed by Mehnert and Cebula (1984) in an internally distributed newsletter from the United States Geological Survey (as cited in Harlan et al., 2005). They reported K—Ar ages of 75 ± 2.3 Ma (2σ) and 72.9 ± 2.1 Ma (2σ) for hornblende and biotite mineral separates from a trachybasalt in the southwestern region of the AHVF. However, Sheriff and Gunderson (1990) later suggested that this sampled unit was likely associated with the Late Cretaceous Elkhorn Mountain volcanic field. In their work, and in Gunderson and Sheriff (1991), a K—Ar bulk rock age of 81.1 ± 3.5 Ma (1σ) from "deep within the volcanic pile" was reported alongside a K—Ar age from biotite within a crosscutting shonkinite dike of 71.2 ± 2.7 Ma (1σ). These age constraints imply that magmatic activity in the AHVF spanned 10 Myrs. From this, Gunderson and Sheriff (1991) assigned an average age of 76 Ma to their reported paleomagnetic pole. In a broader tectonic context, this also serves as one of the few valid reference poles for the apparently rapid polar wander path of North America during the mid-Cretaceous through the Tertiary. Given the importance of this pole (and age), the range of previously reported ages, and the inadequate field-constrained sampling in some earlier studies, Harlan et al. (2005) conducted an extensive field campaign sampling both extrusive and intrusive lithologies in the AHVF, reporting $^{40}Ar/^{39}Ar$ and new K—Ar ages from 13 locations. The results from their study indicate that volcanism in the AHVF began around 76 Ma, with younger $^{40}Ar/^{39}Ar$ ages on intrusives ranging from 74.74 to 73.17 Ma.

Specific lithologies within the AHVF include potassium-rich volcanic rocks (trachybasalts and trachyandesites), which are clinopyroxene-phyric; volcaniclastics characterized by graded ash beds, pyroclastic debris, and matrix-supported breccias and conglomerates; and a wide range of shonkinite, latitic gabbro, and syenite intrusive crystalline rocks occurring as plugs and sills, along with thousands of dikes (Cunningham, 1999; Harlan et al., 2005). Previous studies have noted the radial (or subradial) nature of these dike complexes, with some dikes also interpreted as feeders for the laccoliths to the north (Fig. 3a; Beall, 1973; Whiting, 1977; Hyndman and Alt, 1987).

2.2. Field sites

Shonkinite samples from the AHVF were collected from two roadcut outcrops along the Missouri River (Fig. 3a,b). Site 1 is located at 47°09′22″N, 111°49′37″W on the east bank where a modern cliff face exposes a cross-section through the AHVF's volcanics, volcaniclastics, and intrusives (Fig. 3c). The notable features of this roadcut include grayish-brown to red, poorly sorted, variably competent, alternating layers of volcaniclastic breccias, conglomerates, and ash beds that are cross-cut by shonkinite dikes (Fig. 3c,d). The breccias and conglomerates range in color from red to purple, are matrix-supported, and are characterized by angular to rounded clasts mostly between pebble and cobble size. Clasts are typically gray-green, gray, or gray-brown in color and include shonkinite, latitic gabbro, and basalt lithologies (Fig. 3e). Individual pyroxene crystals are also visible within the volcaniclastics. The ash beds are red to beige with primarily sand to granule-size (with rarer cobble-sized) clasts (Fig. 3e). These dikes are characterized by abundant black, glossy, euhedral pyroxene crystals that range in size from ~0.1 to 1.5 cm on the long axis (Fig. 3f,g), and white, anhedral, mineral-filled, vugs (Fig. 3g). Pyroxene "rosette"-like textures are also present but less common.

Sample site 2 is located at 47°16′28"N, 111°83′59"W. Here, the roadcut outcrop consists of a shonkinite dike that crosses both volcaniclastic conglomerates and porphyritic shonkinite lava flows. The shonkinite dike shares similar color and weathering characteristics with crystals range from 0.1 to ~1.5 cm along the long axis, with the majority ranging between 0.1 and 0.5 cm on the long axis (Fig. 3h). White,

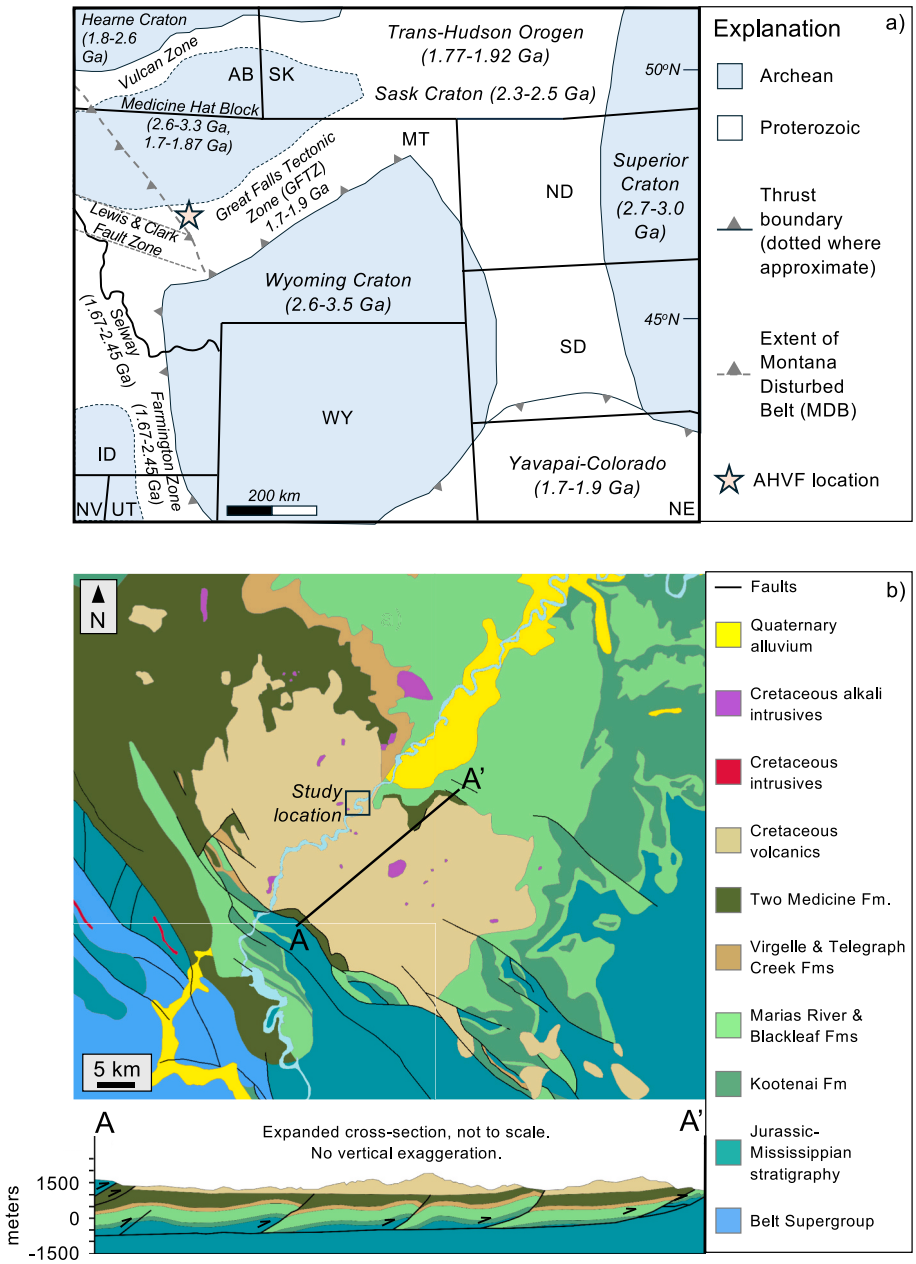

Fig. 2. a) Map showing the location of the Adel Hills Volcanic Field (AHVF) in relation to major basement structures and cratonic boundaries. Modified from Gifford et al. (2014, 2018). Star shows the boundaries of map in b). United States: NV = Nevada; UT = Utah; WY = Wyoming; NE = Nebraska; SD = South Dakota; ND = North Dakota; MT = Montana; ID = Idaho. Canada: AB = Alberta; SK = Saskatchewan. b) Simplified geologic bedrock map and cross section of the AHVF and surrounding area. Map after Vuke (2000, 2014), cross-section after Vuke (2000). All faults are SW-dipping thrust faults unless otherwise indicated. Cross-section datum is mean sea level, vertical to horizontal scales 1:100,000. Cretaceous intrusive rocks include diorite and latite; Jurassic-Mississippian stratigraphy includes Jurassic Morrison Fm, Ellis Group, and Madison Group as well as Mississippian Three Forks, Fm, Jefferson Fm, and Maywood Fm.

mineral-filled vugs are also present (Fig. 3h). The volcanic rocks are a combination of red matrix-supported breccias and conglomerates, gray to red weathered pyroxene-bearing porphyritic lava flows, and a gray blocky lava flow. Similar to site 1, the conglomerates primarily contain shonkinite clasts, with sizes ranging from cobble to granule.

3. Analytical methods

Bulk sample and in-situ mineral characterization were conducted via polarized light microscopy, SEM-EDS, and powder X-ray diffraction (XRD) at Miami University, X-ray fluorescence (XRF) and ICP-MS at Washington State University, EPMA, and LA-ICP-MS at the University of Arkansas. Further details are provided in the Supplementary Tables (S2–S10).

Thin section images were acquired in both plane-polarized light (PPL) and cross-polarized light (XPL) with a Leica DM2700P Petrographic Microscope at MU. The images acquired document the textural and mineralogical features of the samples, aiding in the evaluation of bulk sample characteristics (e.g., modal mineralogies). Subsequently, PLM images were used to identify crystals and areas of petrological interest (e.g., sector and oscillatory zoning in pyroxenes) for further analysis through scanning electron microscope energy-dispersive X-ray spectroscopy (SEM-EDS) and electron probe microanalysis (EPMA).

Initial backscatter electron (BSE) images were acquired using the Zeiss Supra 35 Variable-Pressure Field Emission Gun SEM (VP-FEG-SEM) at MU's Center for Advanced Microscopy and Imaging (CAMI).

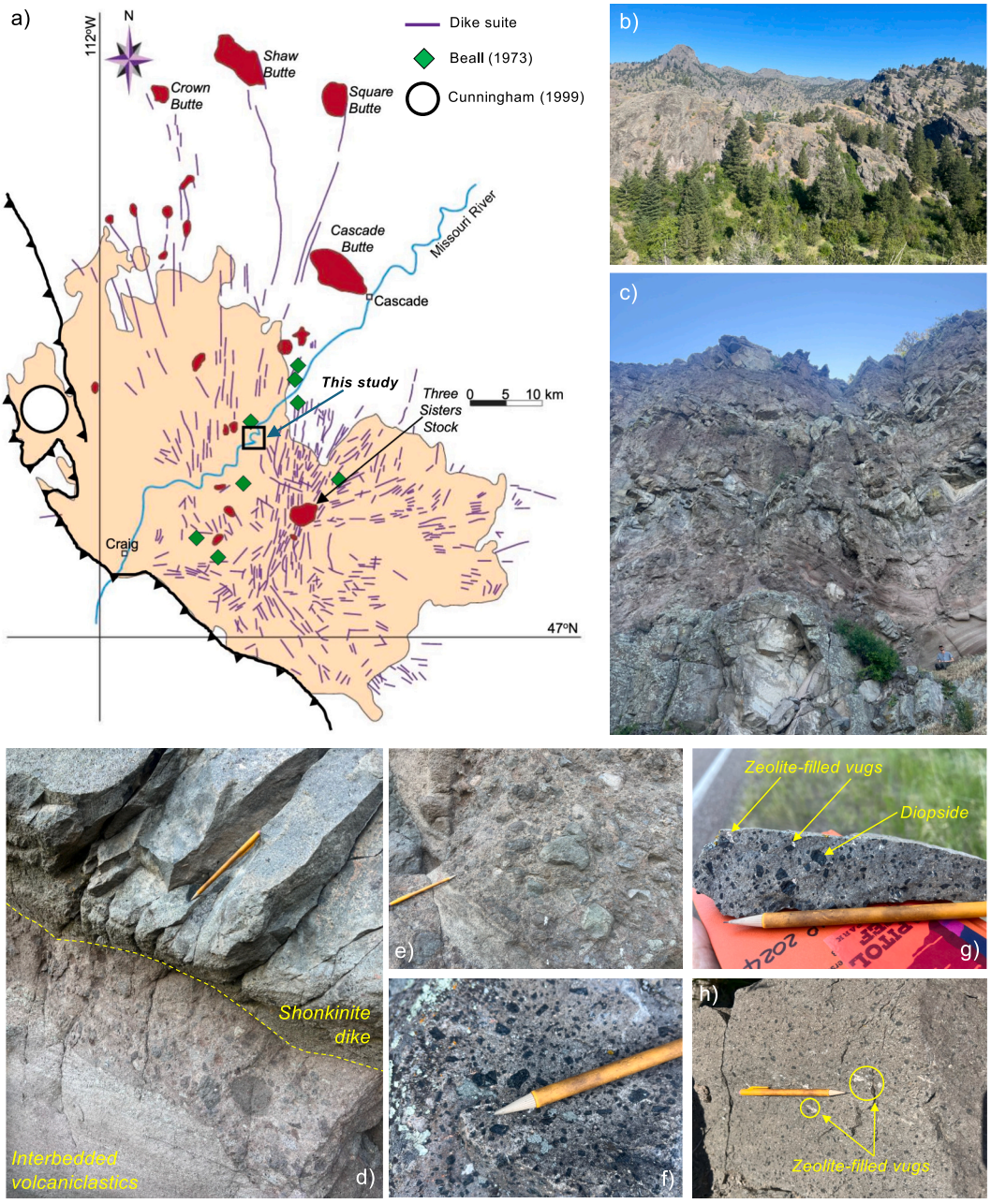

Fig. 3. a) Generalized geologic map with approximate sampling locations across the AHVF from Beall (1973), Cunningham (1999), and this study. Map modified from Lyons (1944). b) view looking west across the AHVF from US highway 15. c) representative photo of multiple shonkinite dikes cross-cutting AHVF volcaniclastics (field site 1). Author Cracas for scale in the lower right. d) close-up of intrusive shonkinite dike cross-cutting the highly variable, interbedded AHVF volcaniclastics. e) shonkinite clasts within a volcaniclastic breccia. f)-g) close up of sampled shonkinite dikes at Site 1 with white, mineral-filled (zeolite) vugs and diopside crystals highlighted. h) shonkinite dike at Site 2, diopside crystals and zeolite-filled vugs also documented.

The images were captured with an accelerating voltage of 25–30 kEV, working distances ranging from 7 to 11 mm, and a 120 μm aperture. Elemental spectra and maps were obtained using the Bruker Xflash 5010 Energy Dispersive X-ray Spectroscope add-on. Both images and elemental data were used to further characterize the sample mineralogy and texture at higher spatial resolutions and to identify regions of interest for subsequent in-situ analyses (e.g., zoned pyroxene crystals). Additional BSE images and accompanying EDS spectra were collected on a Thermo Axia ChemiSEM at the Trace Element and Radiogenic Isotope Lab (TRAIL) at UArk, with an accelerating voltage of 25–30 kEV and a working distance of 10 mm.

The major and minor mineralogy of bulk samples was further evaluated via X-ray diffraction (XRD) on six powdered samples, with three taken from each field site. These powders originated from the same powdered splits prepared for X-ray fluorescence (XRF) at WSU (as detailed later). The powders were run at MU on a Bruker D8 Advance ECO Powder X-Ray Diffractometer equipped with a LYNXEYE XE-T detector using a CuKα radiation ($\lambda = 1.5418$ Å) tube with a 40 kV operating voltage and a 25 mA current. Each sample was analyzed for 110 min, from 4° to 70° 2θ with a step size of 0.01° 2θ and a dwell time of 0.10 s/step.

Major and minor oxide abundances were obtained via bulk powder X-ray Fluorescence (XRF). Analyses were conducted on powdered sample splits from the same six samples characterized by XRD (see above). These samples were processed and analyzed at the Peter Hooper GeoAnalytical Lab at WSU using a ThermoARL Advant'XP+ sequential

XRF spectrometer. 28 g of sample chips were ground in a swing mill with tungsten carbide surfaces for two minutes. 3.5 g of the resulting powder were weighed into a plastic mixing jar with 7.0 g spec pure Li2B4O7 and mixed using a plastic ball for 10 min. The mixed powders were then emptied into graphite crucibles and fused in a muffle furnace at 1000 °C for 5 min. After heating, the glass beads were allowed to cool, then reground in the swing mill for 35 s, placed back in the crucibles, and then refused for 5 min. Following this, the beads were labeled with an engraver, polished with 600 silicon carbide grit, finished with the grit and alcohol on a glass plate, washed in an ultrasonic cleaner, rinsed in alcohol, and dried. XRF analysis was conducted for 27 elements, alongside an integrated analysis of the following USGS standards: AGV-2, BCR-2, and GSP-2. Bulk trace element abundances from the same powders were acquired via inductively-coupled plasma mass spectrometry (ICP-MS). Analyses were conducted at the Peter Hooper GeoAnalytical Lab using the Finnigan Element2 ICP-MS.

In-situ major mineral oxide and minor element data were collected using EPMA. These analyses were conducted using the JEOL JXA-8230 Electron Microprobe at the Chevron Geomaterials Characterization Lab at LSU. Spot analyses were performed on selected pyroxenes, feldspars, iron oxides, and apatites. One pyroxene crystal was chosen for high-resolution elemental mapping. The instrument parameters used were a 5 μm spot size, a 15 kV accelerating potential, and a 20 nA beam current.

In-situ trace element analysis of clinopyroxene and apatites was conducted via laser-ablation ICP-MS (LA-ICP-MS) using the Thermo iCapQ quadrupole mass spectrometer, which is coupled to a New Wave/ESI 193 nm laser ablation system at the TRAIL facility at UArk. Analyzed isotopes included 23Na, 24 Mg, 27Al, 29Si, 39 K, 43Ca, 44Ca, 45Sc, 48Ti, 52Cr, 55Mn, 66Zn, 85Rb, 88Sr, 89Y, 90Zr, 93Nb, 139La, 140Ce, 141Pr, 146Nd, 147Sm, 153Eu, 157Gd, 159 Tb, 163Dy, 165Ho, 166Er, 169Tm, 172Yb, 175Lu, 178Hf, 181Ta, 208Pb, 232Th, and 238 U. For all analyses, the following laser settings were used: a 10 Hz repetition rate over 20s, a laser fluence of ~4.3 J/cm2, and a He carrier gas flow rate of 0.800 L/min. Ablation was performed using a 25 μm laser spot diameter. The instrument was tuned such that UO/U and ThO/Th were < 1.0 %. NIST 612 was used as the calibration standard (see Jochum et al., 2011), with 43Ca as the internal standard for all analyses. Calcium abundances were acquired prior via EPMA analyses of the respective phases. Standards NIST 610 and NIST 612 were run as the primary and secondary standards. Each standard was run before and at the end of each analytical session and was bracketed after every ten analyses during the analytical runs. Data reduction was performed using the Iolite v.4.8.0 Software package (Hellstrom et al., 2008; Paton et al., 2011) and the Trace Elements data reduction scheme. While U—Pb dating of apatite was attempted, the spot size of 50 μm was larger than the targeted grains, resulting in a mixed signal from their host diopsides.

4. Results

4.1. Microscopy (polarized-light microscopy and SEM-EDS)

30 representative hand samples were collected from the field. From six samples (three from Site 1 and three from Site 2) thin sections and bulk powders were prepared. Their petrography was investigated using polarized light microscopy (PLM). Samples from both field sites display large unoriented, small to coarse-grained (0.1–1.3 cm), black, glossy tabular euhedral pyroxene crystals (~25–30 %) within a dark-gray to brown-gray matrix (~70 %); the size and abundance of the pyroxene crystal population vary between field sites, with crystals from Site 1

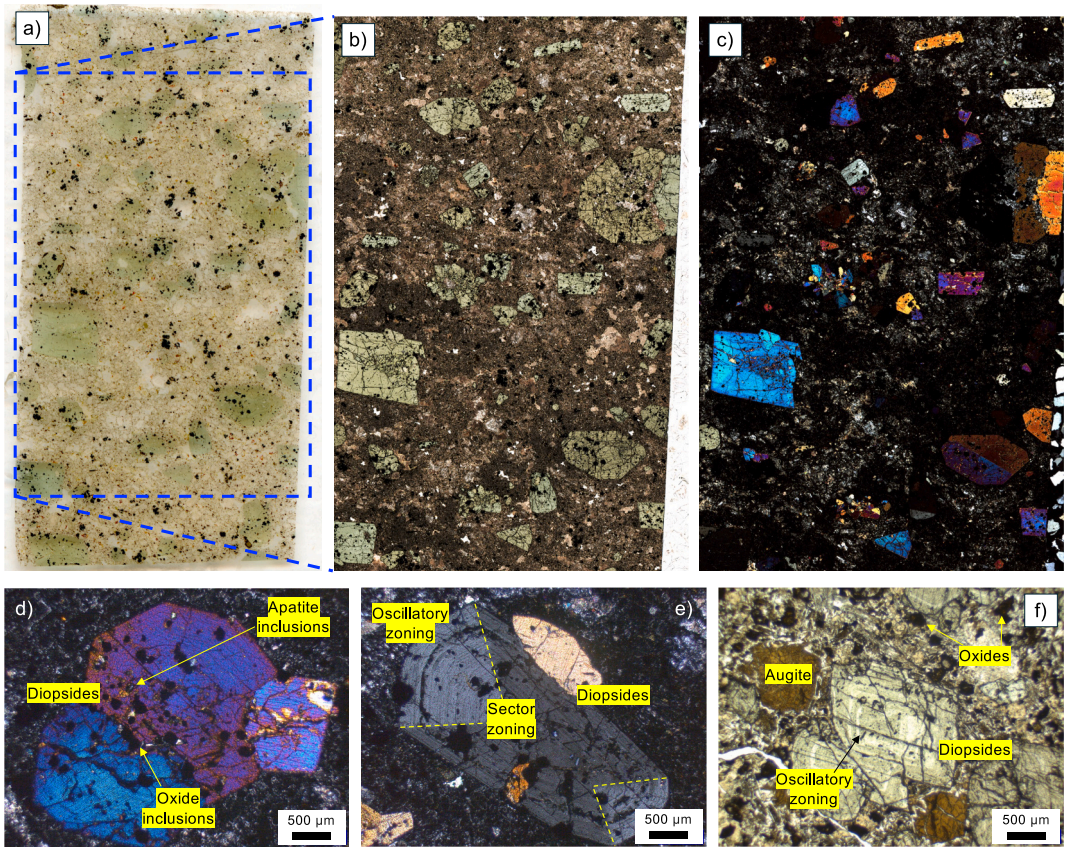

Fig. 4. Summary of major shonkinite petrography. A) Entire thin section photograph. B) high-resolution scan in plane-polarized light (PPL). C) high-resolution scan in cross-polarized light (XPL). D) diopside crystals with apatite and oxide inclusions (XPL, field site 1). E) sector-zoned diopside (field site 1). F) diopside and augite (PPL, field site 2).

being larger on average, ranging from 0.5 to 1.2 cm (Figs. 3f,g,h and 4a, b). From Site 2, pyroxene crystals typically measure 0.1–0.4 cm but can reach up to 1.5 cm (although rare). Shonkinites at both sites contain zeolites as secondary minerals (1–3 %), which is consistent with previous work in the AHVF (Lyons, 1944; Beall, 1973; Cunningham, 1999).

The dominant pyroxene observed at both field locations is diopside (Fig. 4). They were identified by their pleochroic green color in plane-polarized light (PPL, Fig. 4a,b), inclined extinction, sector zoning and their lamellar twinning (Fig. 4c-d). At Site 2, minor augite (<5 %) was also identified by its high relief and brown color in PPL (Fig. 4e). The diopsides from both sites exhibit both hourglass-style sector zoning (Fig. 4d) and oscillatory zoning (Fig. 4c,d). The surrounding groundmass is fine-grained, feldspathic, and altered with anhedral secondary zeolites present often in vugs. Opaque phases, typically euhedral, are also observed in the groundmass and as inclusions within the diopsides alongside trace amounts of apatite (Fig. 4c). Although other inclusions within the diopsides were observed, they could not be unambiguously identified using PLM due to their relatively small sizes. Highly altered amphiboles were observed in the groundmass, displaying significant opacitization. Rare calcite was also observed in the groundmass at Site 2. Additional documentation of sector-zoned diopsides from throughout the sampled shonkinites is provided in Supplementary Fig. 1a-f. A representative image of a vug characterized by secondary zeolites, plagioclase, and calcite is shown in Supplementary Fig. 1g (see also, Fig. 3g,h).

Thin section-scale characterization was also conducted via SEM-EDS. The diopsides exhibit clear oscillatory zoning (Fig. 5a,b) and are interpreted as Al-rich diopsides based on the corresponding EDS spectra. Augites are euhedral, appear darker in backscatter, and show no zoning (see Fig. 5c). The opaque phases observed in PLM, and shown in Fig. 5d, are interpreted as Ti-rich magnetites based on their EDS spectra (confirmed via EPMA, see Section 4.4). These occur as inclusions within diopsides and throughout the groundmass. Their sizes range from ~0.4 μm to >300 μm and make up 30–40 % of the clinopyroxene inclusions. Apatites (as indicated by EDS spectra; Fig. 5d) occur both as inclusions in diopsides (10–30 % of the inclusion population) and within the groundmass. Ca-amphiboles were identified but are uncommon (<1 %) in Site 1 samples and more abundant (<5 %) in Site 2 samples. They are anhedral and display distinct, polymineralic reaction rims (Fig. 5e). Feldspar inclusions in the diopsides were confirmed as both plagioclase

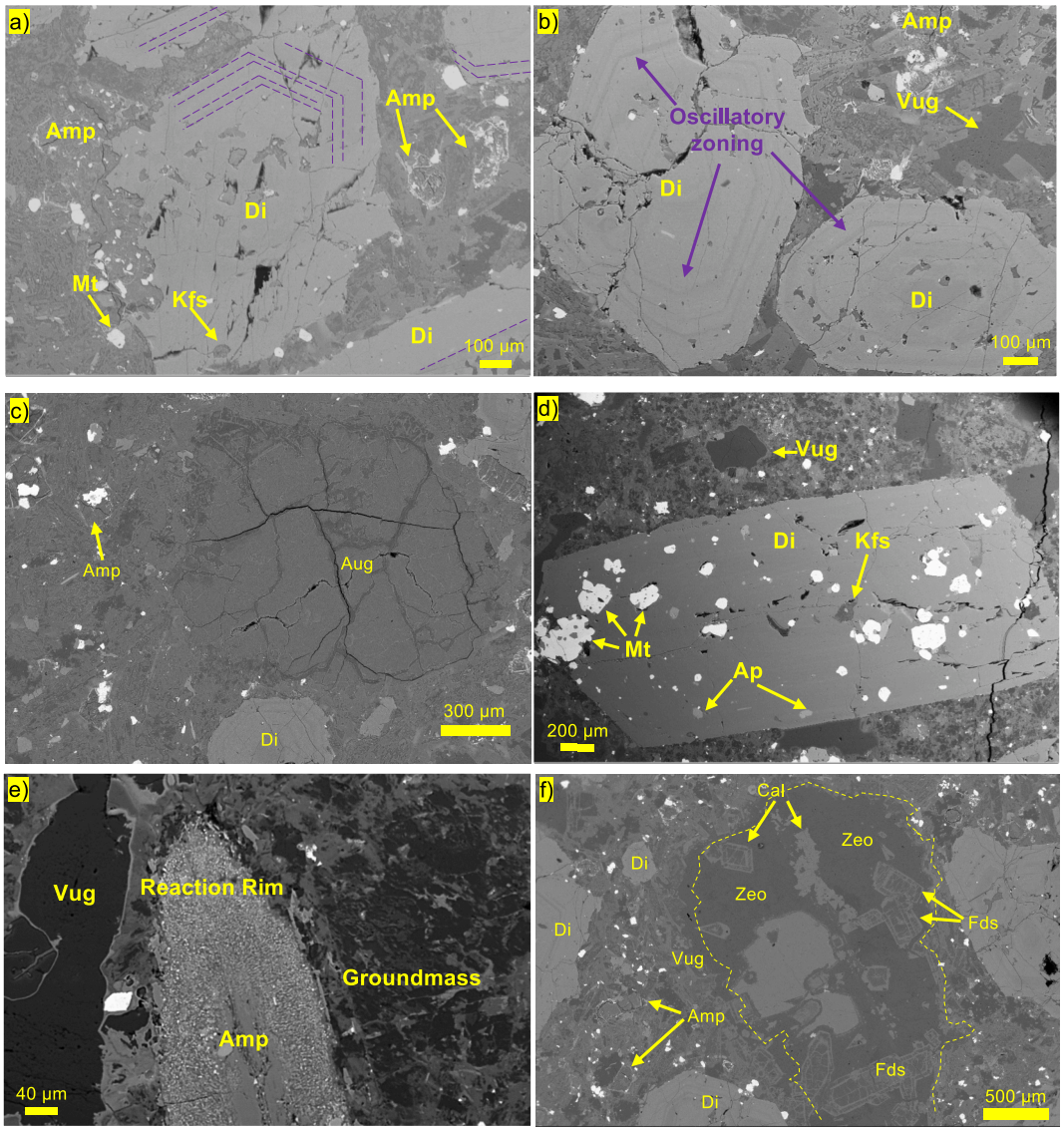

Fig. 5. SEM-BSE images of sampled shonkinites. a) amphibole reaction rim from field site 1. b) diopside with apatite, alkali feldspar, and magnetite inclusions from field site 1. c) oscillatory zoning in diopside, fine-grained groundmass with minor amphibole from field site 1. d) oscillatory zoning in diopside, field site 2. e) vug characterized by calcite, plagioclase, and zeolite, field site 2. f) augite, field site 2.

and alkali feldspar. Plagioclase inclusions range in size from 100 to 500 μm and account for approximately 15 % of the diopside inclusions, while alkali feldspar inclusions range from 50 to 300 μm and also comprise ~15 % of diopside inclusions. At Site 2, other previously unobserved phases included a rare iron sulfide phase, rare biotite, and rare ilmenite. The zeolites identified in hand samples and via light microscopy are associated with complex intergrowths of calcite and plagioclase feldspar (Fig. 5f). Some of these feldspars exhibit oscillatory zonation (Fig. 5f).

4.2. X-ray diffraction

Fig. 6 presents representative results from a single bulk shonkinite powder XRD analysis. Six bulk samples (three from each site) were characterized via XRD and their mineralogies were observed to be the same (see S2). Results are consistent with field-based, PLM, and SEM-EDS observations (see Section 4.1). Diopside is confirmed as the major clinopyroxene while magnetite is identified as the primary iron oxide phase. For diopside, peaks were observed at 29.83 (221¯), 30.33 (310), 30.84 (311¯), 35.72 (221), 39.18 (311), 42.36 (331¯), and 65.74 (531) 2θ (PDF-00-900-5560). Magnetite was identified by 2θ peaks at 35.48 (311), 37.12 (222), and 62.63 (440) (PDF-00-900-2317). Additionally, apatite, K-feldspar, zeolite, and plagioclase were all noted in the XRD patterns, which is again consistent with microscopy and EDS data. These mineral phases are further identified via XRD as fluorapatite, sanidine, analcime, and bytownite, respectively (see Fig. 6). Fluorapatite was identified by 2θ peaks at 31.88 (32¯1), 40.59 (42¯1), 50.69 (53¯1), 56.58 (53¯2) (PDF-00-154-9763). Sanidine was identified by 2θ peaks at 21.08 (201¯), 23.51 (130), 26.92 (220), 32.31 (132¯), and 50.79 (043) (PDF-00-900-8218). Analcime was identified by 2θ peaks at 15.80 (211), 18.27 (220), 25.95 (400), and 30.52 (332) (PDF-00-900-0646). Bytownite was identified by 2θ peaks at 23.52 (131¯), 25.68 (114¯), and 28.47 (220) (PDF-00-901-1201). This data is consistent with previous studies of reported shonkinite mineralogy in the AHVF (e.g., Lyons, 1944; Beall, 1973; Cunningham, 1999; Harlan et al., 2005). Powder diffraction files (PDF) for the minerals identified are provided in Table S3.

4.3. Bulk rock geochemistry

Bulk rock compositional data is presented in Table S4. Fig. 7a shows wt% SiO_2 versus $Na_2O + K_2O$ for the sampled shonkinites, alongside available bulk rock data from previous regional studies (Beall, 1973; Cunningham, 1999). These earlier studies included samples from the western fault block (Cunningham, 1999; Fig. 3a) and from dikes in the south-central and eastern parts of the AHVF (Beall, 1973; Fig. 3a); Cunningham (1999) notes that both early-stage and late-stage intrusion shonkinites were sampled. Samples from Site 1 tightly cluster at ~48 wt % SiO_2 and ~ 8 wt% $Na_2O + K_2O$ within the trachyandesite compositional field. Samples from Site 2 also tightly cluster at ~48 wt% SiO_2 and ~ 6 wt% $Na_2O + K_2O$ between the trachybasalt and basaltic trachyandesite fields. For comparison, samples reported in Beall (1973) range between ~57–66 wt% SiO_2 and ~ 8–12 wt% $Na_2O + K_2O$ across the trachyandesite and trachyte fields. Samples analyzed by Cunningham (1999) range from ~51 to 56 wt% SiO_2 and approximately 8 to 10 wt% $Na_2O + K_2O$ across the basaltic trachyandesite, tephriphonolite, and trachyandesite fields. As seen in Fig. 7b, samples from this study can also be classified as shoshonitic (very high-K) based on their wt% SiO_2 versus wt% K_2O systematics: >3 wt% K_2O at <50 wt% SiO_2. Samples from earlier work by Beall (1973) and Cunningham (1999) are also shoshonitic at >4 wt% K_2O (up to 6.6 wt% K_2O; Fig. 7b). From MgO-FeO*-$Na_2O + K_2O$ ternary systematics, the sampled shonkinites of this study show a calc-alkaline magmatic affinity and are similar to the shonkinites described by Cunningham (1999), (Fig. 7c).

Fig. 8a shows a primitive mantle-normalized multi-element plot that compares shonkinites collected in this study compared to data from Cunningham (1999). Each sample displays relative enrichment in large-ion lithophile elements (LILEs; from K to U), a relative depletion of high field-strength elements (HFSEs; Nb, Ta, Hf, Zr), and an enrichment in Pb. Notably, all samples reveal a well-defined negative Nb—Ta anomaly. Trace element patterns like those observed in this multi-element plot have been interpreted as being consistent with arc volcanism. Fig. 8b shows a chondrite-normalized plot for the AHVF shonkinites compared to the LREE data of Cunningham (1999). All samples are LREE enriched, HREE depleted, and characterized by comparatively flat HREE profiles: La_N/Sm_N = 2.69–5.38, Sm_N/Dy_N = 2.70–2.94, and Dy_N/Lu_N =

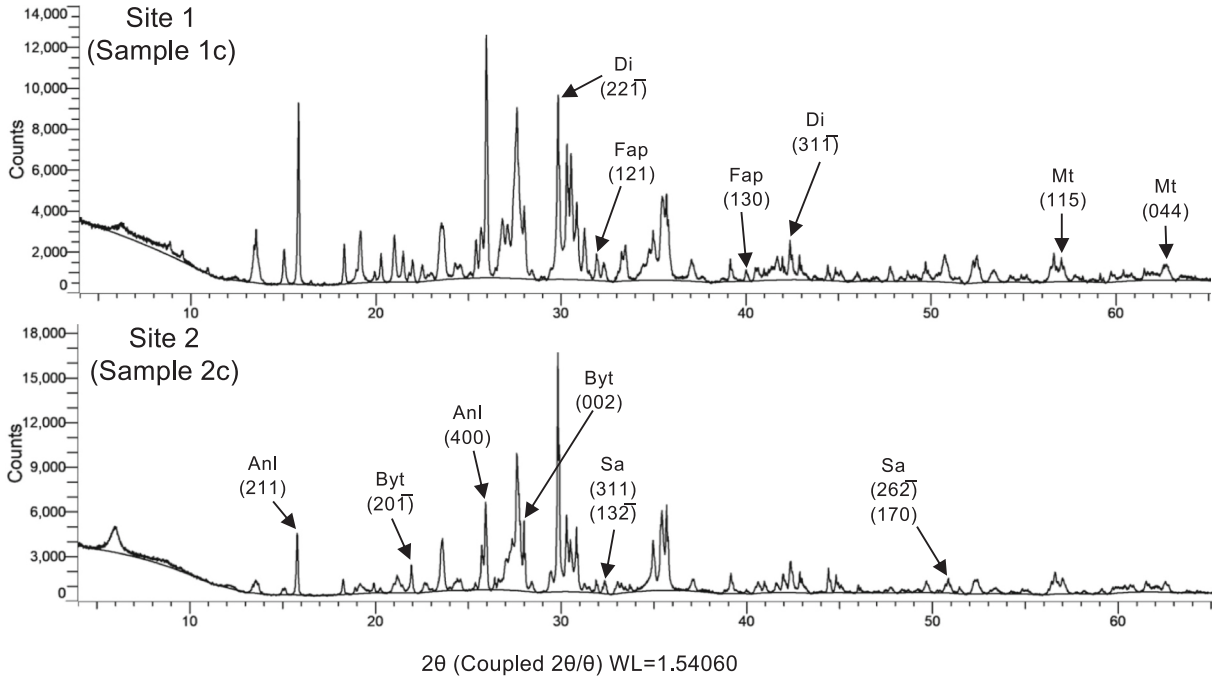

Fig. 6. X-ray powder diffraction (XRD) patterns for this study's shonkinites. All minerals identified are present in all samples: three minerals labeled per pattern for clarity. Di = diopside, Fap = fluorapatite, Mt. = magnetite, Anl = analcime, Byt = bytownite, Sa = sanidine.

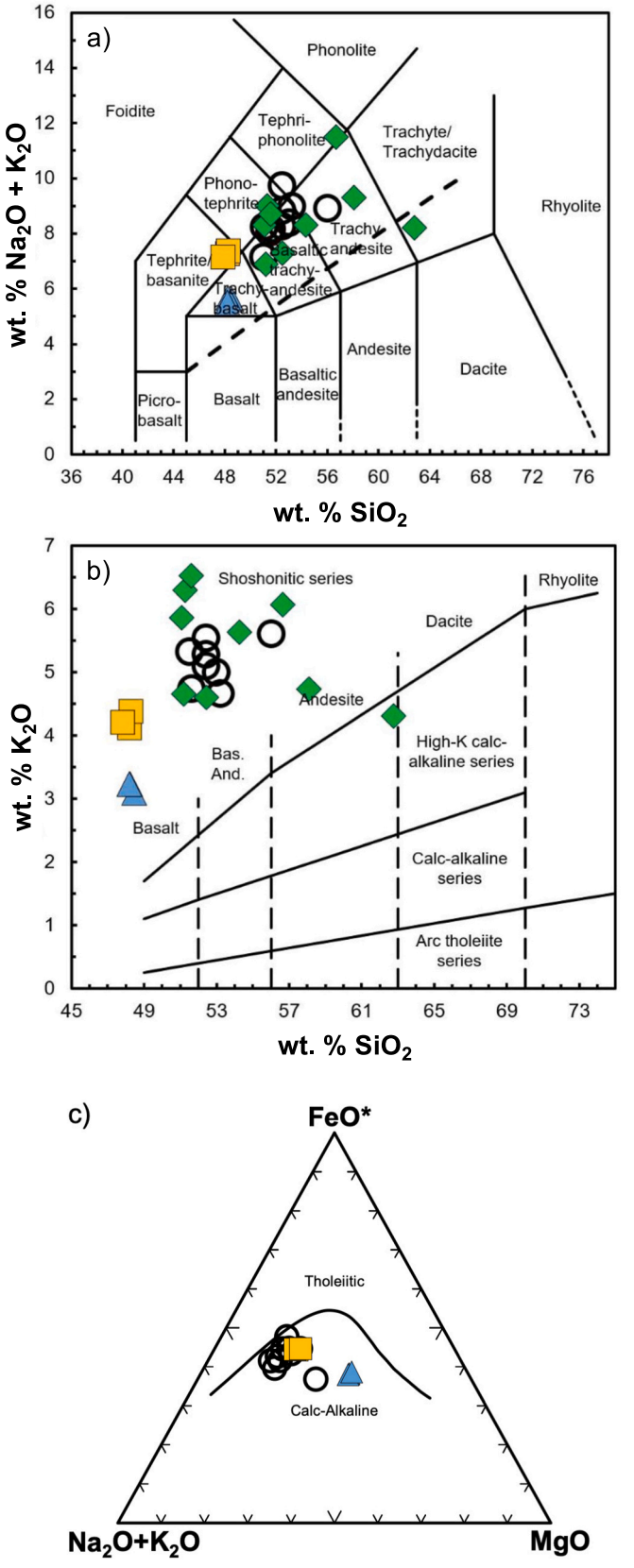

Fig. 7. Major element classification diagrams for shonkinites sampled by this study and those of Beall (1973) and Cunningham (1999). a) TAS plot after LeBas et al. (1986); b) Tholeiitic-calc-alkaline magma series plot after Peccerillo and Taylor (1976); c) AFM diagram after Irvine and Baragar (1971).

1.40–1.44. All samples are characterized by a minor negative Sm anomaly ($Sm/Sm^* = 0.83–0.85$) and a minor positive Eu anomaly ($Eu/Eu^* = 1.12–1.22$).

In summary, the bulk trace element signatures are consistent with the shonkinites being associated with alkali-rich magmas in a volcanic arc system, characterized by LILE enrichment, Nb—Ta depletion and calc-alkaline affinities.

4.4. *In-situ mineral chemistry*

Diopsides, feldspars, apatites, and Ti-rich magnetites were analyzed using EPMA for their major and minor element abundances ($n = 100$; Tables S5–S8). Within the clinopyroxene ternary space, all analyses consistently yielded diopside compositions within the limited range of $Es_{35–42}Fs_{11–17}Wo_{44–48}$ (Fig. 9a). These data are consistent with the PLM, SEM-EDS, and XRD data reported earlier. The wt% Al_2O_3 abundances of diopside range from 2.6 to 6.7, with an average of 3.9 (±1.7, 2σ), while the Mg# values ($Mg/[Mg + Fe^{2+}]$) span from 68.5 to 78.5, averaging 74.2 (±4.3, 2σ).

Feldspars analyzed via EPMA represent feldspar populations in the groundmass and those present as inclusions within diopsides (Table S6). Feldspars show a range of compositions that are generally consistent with XRD results. This includes plagioclase (predominantly bytownite) and anorthoclase (K-rich albite) with compositions close to that of sanidine. Plagioclase feldspars ($n = 15$) range from $An_{96}Ab_2Or_2$ (anorthite) to $An_{15}Ab_{85}Or_0$ (oligoclase) with the majority being bytownite ($n = 8$). Potassium feldspars ($n = 9$) specifically range from $An_3Ab_{67}Or_{30}$ (anorthoclase) to $An_4Ab_{10}Or_{86}$ (sanidine).

Sixteen apatites, present as inclusions within diopsides, were analyzed via EPMA, with OH calculated using the method proposed by Ketcham (2015), (Table S7). The shonkinite apatites consistently plot as fluorapatites (Fig. 9b). Fluorine contents range from 2.71 to 3.75 wt%, while Cl contents are an order of magnitude lower, ranging from 0.46 to 0.88 wt%. Calculated OH contents vary between 0.00 and 0.62 wt%. Using the apatite ternary diagram of McCubbin et al. (2011), the shonkinite apatite grains plot within fields indicate that melt F and/or Cl are greater than H_2O. Twelve Ti-rich magnetites from the groundmass and those found as inclusions within the diopsides were analyzed using EPMA (Table S8). The data is consistent with near-endmember magnetite compositions.

Selected diopsides and apatites were analyzed for their trace element abundances using LA-ICP-MS. Data are provided in Tables S9 and S10, respectively. Fig. 9c shows rare earth element chondrite-normalized profiles, with all diopsides exhibiting an S-curve profile. Shonkinite diopsides display variable depletion in LREEs ($La_N/Sm_N = 0.47–1.03$), MREE enrichment ($Sm_N/Dy_N = 2.30–2.37$), and relatively flat HREE profiles ($Dy_N/Lu_N = 1.64–1.91$; Fig. 9c). A minor Sm anomaly is also detected ($Sm/Sm^* = 0.83–1.06$). Calculated Eu anomalies in sampled diopsides range from 0.92 to 1.33 however, only 3 analyses are <1 (average $Eu/Eu^*: 1.12 \pm 0.15$ 2σ). Shonkinite apatites show enrichment in REEs ranging from 30 to 1000 times that of chondrite and exhibit an LREE-enriched profile: $La_N/Sm_N = 2.14–2.37$, $Sm_N/Dy_N = 3.65–4.03$, $Dy_N/Lu_N = 2.59–3.18$ (Fig. 9d). Minor negative Sm anomalies and consistently positive Eu anomalies are also noted ($Sm/Sm^* = 0.85–0.89$; $Eu/Eu^* = 1.03–1.10$).

High-resolution, elemental mapping was performed on one selected diopside crystal via EMPA. The element map was collected by EDS at an accelerating potential of 15.0 kV with a beam current of 50.0 nA, a dwell time of 25 ms, and a step size of 2.0 μm. The resulting elemental maps reveal significant sector and oscillatory zoning with respect to Si, Fe, Mg, Ca, and Al (Fig. 10). The mapped crystal reveals low Al, high Si, and high Mg 'hourglass' sectors {−111}, alongside adjacent high Al, low Si, and low Mg 'prism' sectors {*hk*0}. See discussion later.

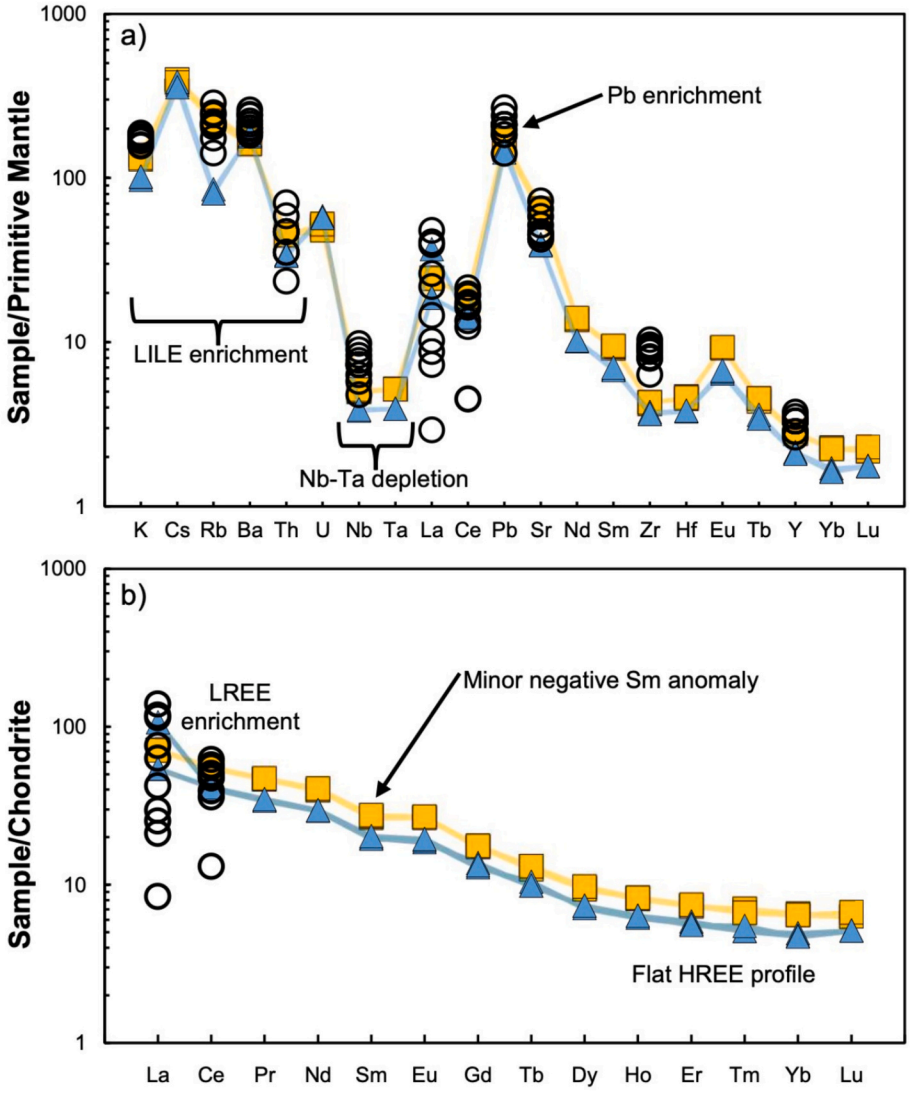

Fig. 8. Trace element spidergrams for AHVF shonkinites, a) primitive mantle-normalized and b) rare-earth element (REE) data normalized to chondrite. Values for primitive mantle and chondrite reservoirs from Sun and McDonough (1989). Symbology as in Fig. 6.

5. Discussion

In the following discussion, crystal-scale observations from the AHVF shonkinites are used to evaluate their petrogenesis, with interpretations later placed into a regional and global tectonomagmatic framework. Collectively, this detailed petrological study and a review of shonkinite occurrences globally are used to propose a petrogenetic model for shonkinite magmatism during the Cretaceous in the AHVF.

5.1. Clinopyroxene sector zoning

Clinopyroxene can record a variety of processes related to magmatic evolution, such as crystallization, magma storage, ascent, and eruption conditions (e.g., Chen et al., 2018; Ubide et al., 2019; Zhou et al., 2021; Qu et al., 2024). It has been established that the crystallization of clinopyroxene is sensitive to variations in magmatic temperatures, pressures, and H_2O contents (e.g., Neave and Putirka, 2017; Putirka, 2017; Mollo et al., 2018). For instance, clinopyroxenes have been utilized in diffusion chronometry studies, using their oscillatory growth patterns to determine timescales ranging from hours to years or even decades between the intrusion of magma at depth and its eventual eruption (e.g., Costa et al., 2020). While rare in nature, clinopyroxenes can develop either dendritic or skeletal forms (e.g., Ni et al., 2014; Masotta et al., 2020; MacDonald et al., 2022) where the specific growth pattern is influenced by the degree of undercooling.

Kinetic effects operating during clinopyroxene crystal growth can result in prominent sector zoning (e.g., Dowty, 1976; Ubide et al., 2019; Zhou et al., 2021). These sectors can be categorized as “hourglass” for the basal {−111} sectors which grow more rapidly along the crystallographic *c* axis, and “prism” for the {100}, {010}, and {110} sectors which grow perpendicular to the crystallographic *c* axis (Ubide et al., 2019; Zhou et al., 2021). An idealized model of sector zoning in diopside is shown in Fig. 11a.

The driving force behind these sector growths is understood to be linked to magmatic undercooling (represented as ΔT). The extent of undercooling (ΔT) refers to the difference between the final temperature at which crystallization of the mineral of interest occurs and that of the mineral’s liquidus temperature (Kirkpatrick et al., 1981). Cooling or degassing within magma can drive a system to experience undercooling conditions, which initiates crystal nucleation due to newfound thermodynamic favorability (e.g., Mollo and Hammer, 2017). After crystal nucleation occurs, particularly in the context of clinopyroxenes, the degree of magmatic undercooling will determine the overall composition of the crystal as well as that of the discrete sectors during crystal

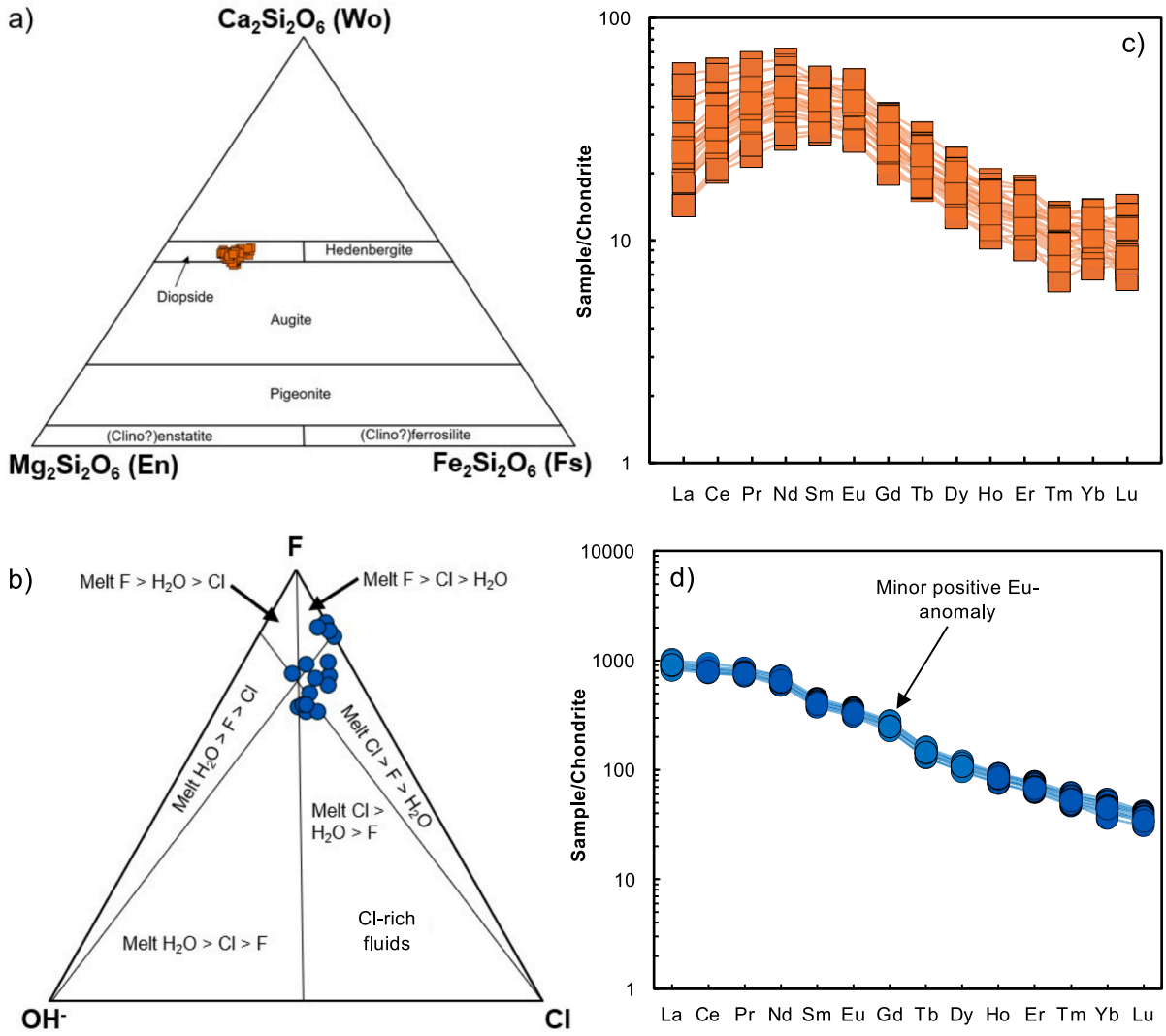

Fig. 9. a) clinopyroxene ternary (n = 100). b) apatite ternary after McCubbin et al. (2011), (n = 16). c) chondrite normalized rare-earth element spidergram for diopsides (n = 89). d) chondrite normalized rare-earth element spidergram for apatites (n = 12). Values for chondrite in c) and d) after Sun and McDonough (1989).

growth (see Fig. 11a; e.g., Zhou et al., 2021). At lower degrees of undercooling (i.e., in scenarios where the liquidus temperature and system temperature are closely aligned), interface-controlled, near-equilibrium growth occurs, resulting in polyhedral crystals (Herring, 1951). At higher degrees of undercooling, crystal growth becomes more rapid and disequilibrated, leading to textural disequilibrium and the formation of skeletal or dendritic crystal morphologies (Ni et al., 2014; Masotta et al., 2020). Experiments have demonstrated that at small degrees of undercooling (where $\Delta T = 13–25$ °C), the {−111} hourglass sector of diopside tends to be relatively enriched in Si and Mg, while the prism sectors tend to be relatively enriched in Al and Ti (Kouchi et al., 1983; Masotta et al., 2020). At higher degrees of undercooling (where $\Delta T > 40$ °C), dendrites that are relatively enriched in Al and Ti can be observed, surrounded by regions enriched in Si and Mg. In this scenario, the contacts between crystal sectors are irregular (Masotta et al., 2020; Zhou et al., 2021; MacDonald et al., 2022).

As shown in Fig. 10, the mapped diopside crystals from the AHVF shonkinite reveals well-defined sector zoning with low Al, high Si and high Mg hourglass sectors. The AHVF crystals display a {−111} hourglass zone characterized by Al depletion (see Fig. 10a) along with relative enrichment in Si and Mg (see Fig. 10c, d). Although only one elemental map at high resolution was acquired, the observed patterns align with a well-established trend of Si and Mg enrichment alongside Al, Ti depletion on {−111}, contrasted with relative enrichment of Al, Ti, and depletion of Si and Mg on the prism sectors (see also Zhou et al., 2021).

As summarized in Ubide et al. (2019), the following cation exchange between the hourglass {−111} sector and the prism sectors has been proposed: $[Si^{4+} + Mg^{2+} + Fe^{2+}]_{-111} \leftrightarrow [Al^{3+} + Ti^{4+} + Fe^{3+} + Na^{2+} + Cr^{3+}]_{hk0}$ to account for the sector zoned chemical patterns of depletion and enrichment (when observed). Given the observed chemical differences described between the diopside sectors, this implies that the AHVF magmatic system experienced low degrees of undercooling (ΔT = 13-25 °C) as outlined in Kouchi et al. (1983) and Masotta et al. (2020). The apparent lack of dendritic growth patterns at the Al sector boundaries (Fig. 10a) are consistent with this interpretation (Zhou et al., 2021). In addition, no clear color ramp difference is observed for Ca or Fe, which is consistent with the cation exchange process discussed.

While only one high resolution elemental map was acquired as part of this study, the above chemical framework can be further evaluated by the EPMA data that was collected from multiple crystals and sectors (n = 89 analyses; Fig. 9a). Fig. 11b and c summarize the wt% SiO_2 vs. Al_2O_3 and wt% SiO_2 vs. MgO systematics respectively. As shown, relative enrichment in Si and Mg is consistently accompanied by relative depletion in Al and Ti. In supplementary fig. S4, wt% SiO_2 vs. TiO_2, FeO, and Na_2O systematics are summarized where wt% Na_2O is the least well

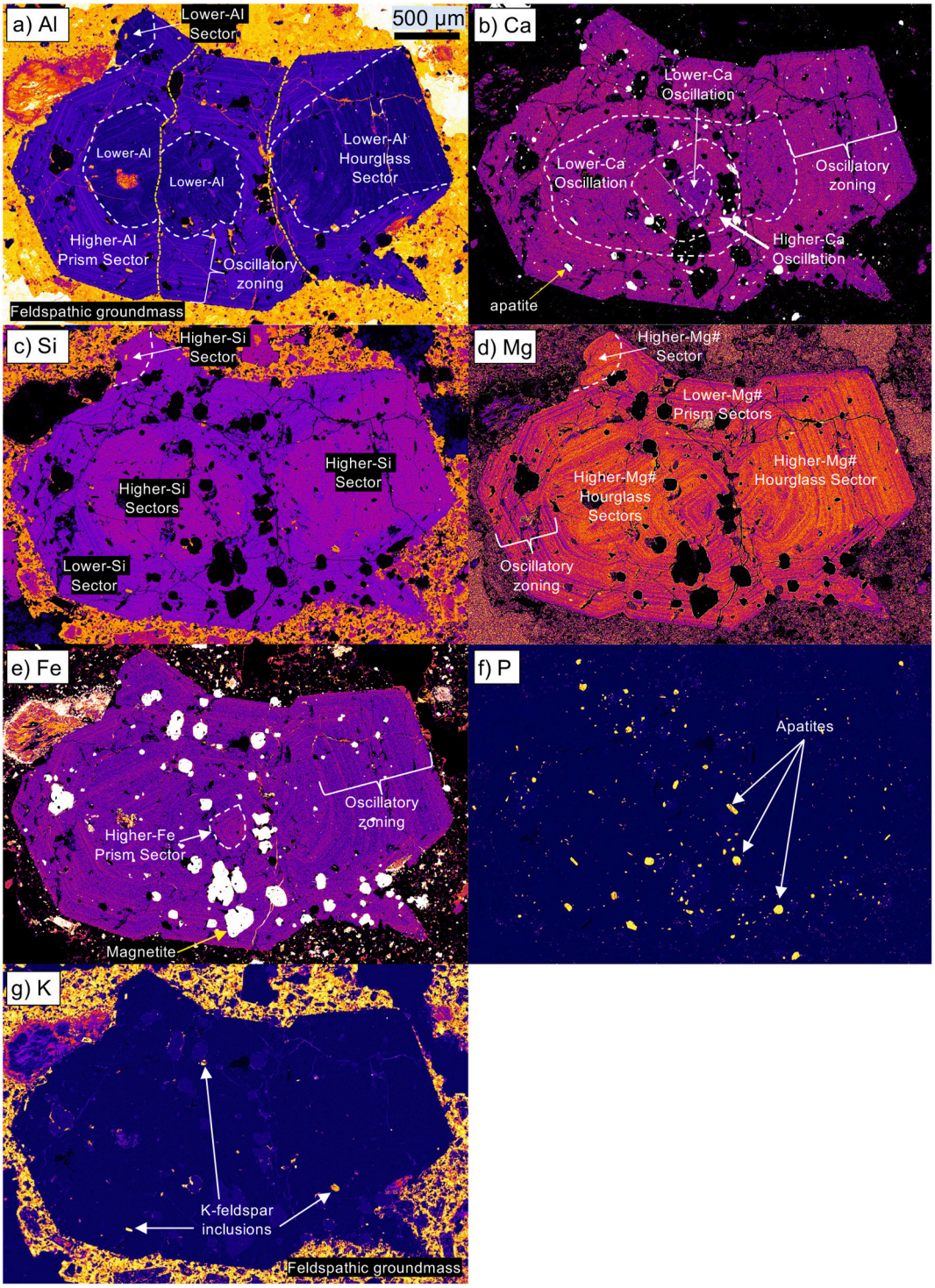

Fig. 10. Elemental maps acquired via EPMA of one select, representative, diopside crystal from field site 1. Brighter, lighter colors indicate relatively high element abundances while darker colors indicate relatively low element abundances. See text for discussion.

correlated with wt% SiO_2, which is consistent with the weak sector partitioning of Na (Ubide and Kamber, 2018).

5.2. *Apatite as a shonkinite petrogenetic indicator*

Apatite has been established as an excellent tracer of magma petrogenesis due to its ability to incorporate petrogenetically useful trace elements (including the REEs), which are collectively sensitive to the magmatic environment in which they formed (e.g., Zafar et al., 2019; Bruand et al., 2020; Zhang et al., 2020; Kieffer et al., 2023). Much of the recent advances in applying apatite trace element chemistry to magmatic processes has focused on its applications to felsic magma evolution and granite petrogenesis, where elemental abundances and ratios are used to categorize apatites into the "granite alphabet" (e.g., Zhang et al., 2020; Kieffer et al., 2024a). However, recent studies have also demonstrated the utility of apatites as tracers of mafic magma provenance (Pedersen et al., 2021; Kharkongor et al., 2023; Kieffer et al., 2023, 2024b). Specifically, the recent work of Kieffer et al. (2024a,

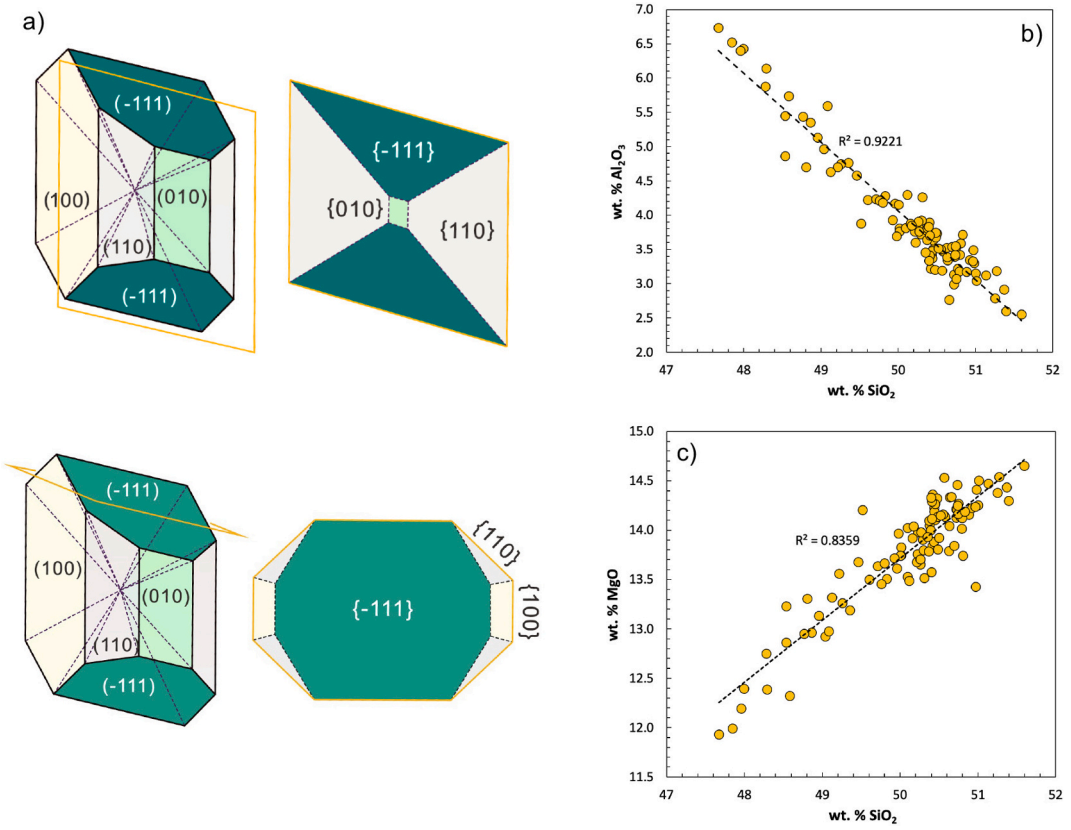

Fig. 11. a) sector zoning in model diopsides modified from Zhou et al. (2021). Prism sectors: {100}, {110}, and {010}, hourglass sector {−111}. b) wt% SiO_2 vs. wt% Al_2O_3 in shonkinite diopsides. c) wt% SiO_2 vs. wt% MgO in shonkinite diopsides. Additional wt% SiO_2 vs. major oxides are provided in Fig. S4.

2024b) developed a series of discrimination diagrams based on fluorapatite trace element geochemistry to better differentiate apatite from felsic, mafic, and even carbonatitic intrusions. Petrogenesis of the AHVF apatites are therefore suitable for use within this framework.

The AHVF shonkinite apatites analyzed via EPMA and LA-ICP-MS in this study are all inclusions within diopsides (e.g., Figs. 5d, 10f). Based on wt% FeO and wt% MgO (not shown), they are demonstrably associated with crystallization from a relatively mafic magmatic system with wt% FeO > 0.1 at wt% MgO > 0.01 compared to apatites in felsic systems where wt% FeO extends to <0.1 at wt% MgO < 0.01 (Rakhimov et al., 2022). In Fig. 12a-e, apatites are plotted within the geochemical frameworks of Kieffer et al. (2023, 2024b). Generally, trace element data are all consistent with a mafic, alkali-rich melt origin. For example, in Fig. 12a, Y (ppm) vs. Sr (ppm) reveals AHVF apatites to be geochemically similar to carbonatites. In the ΣLREE–Sr/Y framework (Fig. 12b) the AHVF apatites fall between the ultramafic (UM) and I-type granitoid/mafic igneous rock field (IM). Considering the Sr/Y-(ΣREE+Y)/10,000-Eu/Eu* framework (Fig. 12c), a mafic to carbonatite affinity is defined.

As outlined in Belousova et al. (2002), Ce^{3+} and Eu^{3+} have ionic radii closer to that of Ca^{2+} than Eu^{2+} and Ce^{4+}. This means Ce^{3+} and Eu^{3+} will more readily substitute into the apatite crystal structure (for Ca^{2+}). In a more oxidizing magmatic environment, the abundance of Ce in apatite will be lower, and the abundance of Eu in apatite will be higher, compared to relatively more reduced magmatic environments. Therefore, the relationship between Ce/Ce* and Eu/Eu* can be used to evaluate the oxidation state of the primary magma (e.g., Miles et al., 2014; Zhang et al., 2020; Khan et al., 2025). The AHVF apatites show Ce/Ce* ranges from 0.92 to 1.02 at Eu/Eu* values of 1.03 to 1.10 (minor positive Eu anomalies as noted earlier). Collectively, these are consistent with apatite crystallization in a moderately oxidized magmatic environment (Fig. 12d). The relative consistency of Eu/Eu* values in shonkinite apatites, compared to Ce/Ce*, is also indicative of a magmatic environment in which oxygen fugacity is relatively stable (Rakhimov, 2024; Khan et al., 2025).

In order to further evaluate the lack of a negative Eu-anomaly in shonkinite AHVF apatites (and clinopyroxenes), the role, or lack thereof, of plagioclase crystallization in the magmatic system must also be considered. Apatite Eu anomalies are significantly influenced by the plagioclase crystallization as plagioclase will sequester Eu^{2+} (along with Sr^{2+}) as Ca^{2+} is replaced (e.g., Bromiley, 2021). In highly oxidizing, hydrous magmatic environments, Eu^{3+} will more readily partition into apatite than plagioclase while the hydrous nature of the system can also contribute to the suppression of the plagioclase liquidus (e.g., Bromiley, 2021; Chen et al., 2023; Kieffer et al., 2023; Khan et al., 2025). These oxidizing, hydrous magmatic conditions as inferred from apatite trace element are consistent with the calc-alkaline affinity of the shonkinites' bulk geochemical signatures and the volcanic arc setting, and likely accounts for the lack of significant negative Eu anomalies within apatite, clinopyroxenes (Fig. 9c,d), and bulk rock signatures (Fig. 8b).

5.3. Comparison of global shonkinite occurrences and petrogenesis

As summarized earlier, shonkinites are rare types of alkali igneous rocks that are found throughout different tectonic settings (e.g., Shadenkov et al., 1990; Petrovskii et al., 2014; Ghodke et al., 2018; Okrugin et al., 2018). Like many classifications, "shonkinite" can exhibit variations both within and between localities. Here, the occurrence of shonkinite in the global geologic record is discussed and the proposed petrogenetic formation models are explored. A summary of the minerals associated with the global shonkinite occurrences discussed below and can be found in Table S1.

The oldest shonkinite occurs in the Kola Alkaline Province on the Kola Peninsula, Russia (Fig. 1; U—Pb zircon analyses from 1.67 Ga to

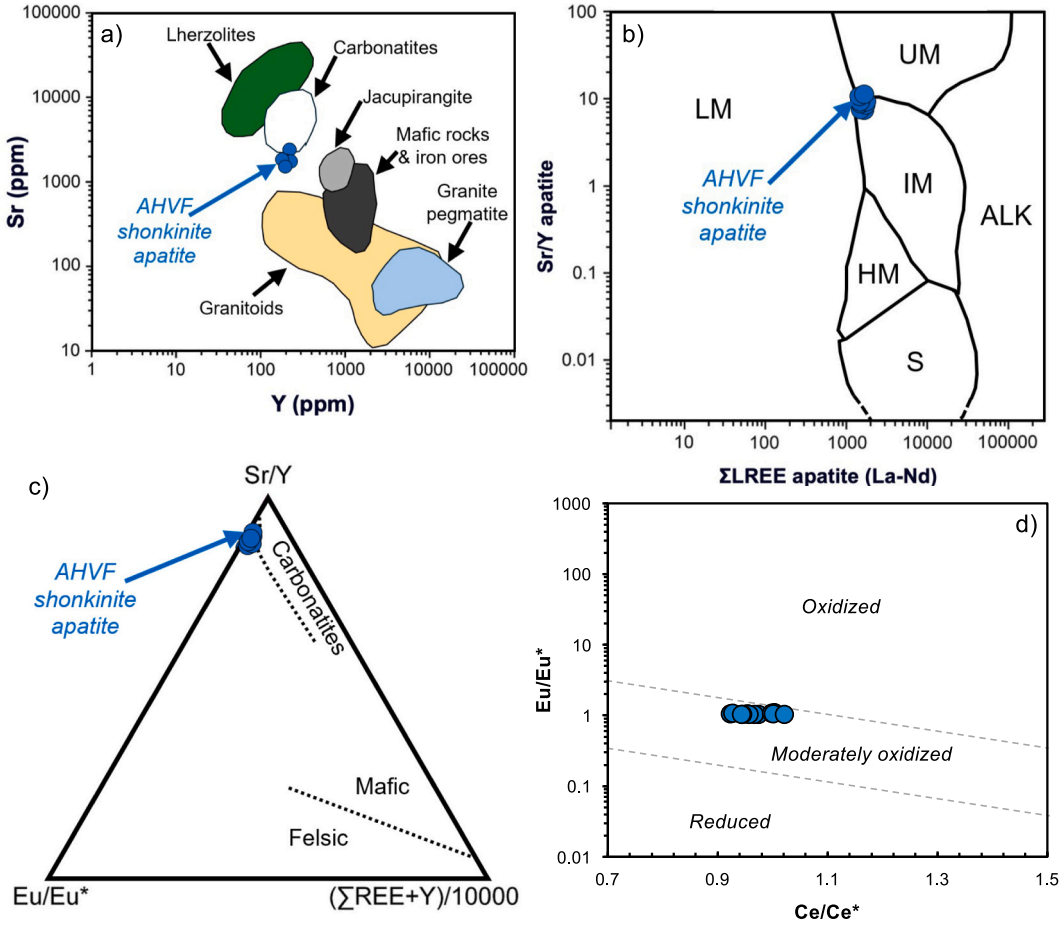

Fig. 12. Apatite chemical affinity diagrams. a) Y—Sr framework after Rakhimov et al. (2022). b) ΣLREE – Sr/Y framework after O'Sullivan et al. (2020). c) Sr/Y – (ΣREE+Y)/10,000 – Eu/Eu* framework after Kieffer et al. (2024a, 2024b). d) Ce/Ce* vs. Eu/Eu* framework after Khan et al. (2025).

1.58 Ga; Petrovskii et al., 2014; Mikhailova et al., 2019). Shonkinites within this region occur as part of a shonkinite-malignite series within a larger complex of nepheline-bearing alkalic igneous rocks with the shonkinitic rocks located near the bottom of the laccolith (Mikhailova et al., 2019). The different alkali rocks within this complex are interpreted to have formed via fractional crystallization along a nepheline-enrichment, clinopyroxene-depletion trend (Mikhailova et al., 2019). Elsewhere, the shonkinites occur as part of a K-enriched peridotite-shonkinite intrusive series From bulk rock Sr—Nd (-εNd, +εSr) isotopic systematics, Petrovskii et al. (2014) propose that the primary melts for the peridotite–shonkinite series were derived from the EM II mantle source reservoir.

The Mountain Pass locale is a moderately dipping, tabular, intrusive complex in south-central California, which is interpreted to have been preferentially emplaced along a zone of lithospheric weakness (Denton et al., 2020). Here, Mesoproterozoic alkali-rich rocks intrude a Paleoproterozoic block and outcrop as a narrow belt for ~130 km (Castor, 2008; Denton et al., 2020). This complex includes carbonatite, shonkinite, ultrapotassic syenite, and alkali granite (Watts et al., 2021; Watts and Andersen, 2025). Notably, the Sulfide Queen carbonatite contains a significant rare-earth element orebody and contributes to Mountain Pass being the second largest REE deposit in the world (after Bayan Obo in Inner Mongolia, China; Castor, 2008; Verplanck et al., 2016; Gadea et al., 2024; Benson et al., 2025). From the work of Poletti et al. (2016), it was concluded that while the carbonatite and ultrapotassic units (including the shonkinites) shared a mantle source and temporal similarity, they were generated during distinct partial melting events as there was no evidence for liquid immiscibility between the units and evidence for fractional crystallization from a common primary melt was also not observed.

From Watts et al. (2021), shonkinite magmatism is proposed to have resulted from partial melting of a heterogenous metasomatized mantle source over millions of years with the metasomatic event constrained to <1.5 Ga. $\delta^{18}O$ signatures of primary zircon populations support a shonkinite generation model in which alkali-rich magmas were derived from metasomatized mantle source (with elevated REE, F, Ba) and experienced crustal assimilation via interaction with a wide range of overlying Paleo- and Mesoproterozoic crustal lithologies. While these data provide a geochemical context, the tectonic context of Mountain Pass is less well constrained with magmatism in the orogenic and contractional settings proposed (e.g., Anderson and Bender, 1989; Whitmeyer and Karlstrom, 2007). More recently, Poletti et al. (2016) favored an orogenic environment, given the occurrence of alkali-rich systems in other contractional settings worldwide. Most recently, Benson et al. (2025) reported bulk rock εNd_i signatures at -2.2 ± 0.8, and εHf_i signatures in zircon $0.1 \pm 1.1$for the Mountain Pass Intrusive Suite, which are proposed as consistent with alkaline and carbonatitic melts being derived from a common mantle source and not through liquid immiscibility. This mantle source is further proposed to have been influenced by the subduction of carbonate-bearing sediments ~300 Myrs before the emplacement of the Intrusive Suite.

The Elchuru alkaline pluton occurs within the larger Prakasam Alkaline Province (PAP) of India's Eastern Ghats region and is cross-cut by a sequence of shonkinite, lamprophyre (minette variety), and dolerite dikes (Madhavan et al., 1992; Ghodke et al., 2018). Magmatism occurred from 1.35 to 1.20 Ga and is associated with the development of a Mesoproterozoic continental rift system at the time of supercontinent breakup along cratonic margins and is characterized by alkaline and

tholeiitic magmatism (Vijaya Kumar and Ratnakar, 2001; Upadhyay et al., 2006; Upadhyay, 2008; Vijaya Kumar et al., 2011; Ghodke et al., 2018). Within the Elchuru pluton, shonkinite dikes occur in a swarm perpendicular to the rift axis (Ghodke et al., 2018). Early work by Madhavan et al. (1992) proposed that the shonkinite magma represented a primary melt, which then differentiated to form the different rock types throughout the pluton. From more recent work by Upadhyay et al. (2006), it was proposed that PAP alkaline magmas originated from an enriched mantle source region within the subcontinental lithosphere which was metasomatized between 1.9 Ga and 2.1 Ga (from t_{DM} Nd model ages).

The Salem Block of the Southern Granulite Terrane (SGT), near the southernmost tip of the Indian subcontinent, formed during the Neoarchean and was later metamorphosed in the early Paleoproteozoic (Anderson et al., 2012). These plutons are inferred to have been emplaced along a transcrustal zone within the SGT which represents a failed rift caused by slab pull during assembly of Gondwana (Renjith et al., 2014; Santosh et al., 2014; He et al., 2015, 2016; He et al., 2018; Boraiaha et al., 2020). The Neoarchean Salem Block sits in the north-center of the SGT and is composed mostly of metamorphic lithologies with shonkinites and other ultramafic lithologies occurring along an *E*-W trending zone which is coincident with the site of the proposed failed rift (He et al., 2018). Shonkinite primary magmas are inferred to be derived from the partial melting of a metasomatized lithospheric source in a continental rift setting. The age of shonkinite magmatism was constrained by U—Pb dating of zircons at 818 Ma (± 6.3; He et al., 2015).

The early Cretaceous shonkinites of the Aldan Shield in western Siberia occur at three distinct localities; the MalyyMurun pluton, Ryabinovyi Massif, and Inglali Massif (Shadenkov et al., 1990). The MalyyMurun pluton, where shonkinite occurs with pyroxenite and syenite varieties, formed as a lopolith between two sedimentary layers of Mesozoic strata (Orlova, 1987; Shadenkov et al., 1990). Here, the shonkinites are proposed to have formed via fractional crystallization from a high-alkali, high-Ti, high-REE, high-volatile melt (Shadenkov et al., 1990). The Ryabinovyi Massif, where the shonkinites occur as necks and dikes within a complex series of high-alkaline intrusive and extrusive rocks within a caldera, are proposed to have formed from an alkali-rich, ultramafic, carbonate-silicate melt from a "deep-seated" mantle source (Rokosova and Panina, 2013). Rokosova and Panina (2013) further proposed that during early diopside crystallization of the biotitic shonkinites, liquid immiscibility between silicate, carbonate-salt, and carbonate melts occurred, supported by the presence of calcite-bearing carbonatite veins (Kochetkov, 2006) and carbonate-salt inclusions within shonkinite clinopyroxenes The Inglali Massif, where shonkinites occur alongside ultramafics, varieties of syenites, and pulaskites in a concentric ring around the core of the massif, are interpreted to represent a single and continuous comagmatic series (Rokosova et al., 2016; Okrugin et al., 2018). Formation of the massif is constrained to the Jurassic-Cretaceous with an early Cretaceous zircon U—Pb age for the shonkinites at 120 ± 2 Ma (Okrugin et al., 2018). From the work of Bogatikov et al. (1994), it was suggested that the central region of the Aldan Shield formed from a relatively depleted, heterogeneous mantle source, which was influenced by subduction,as indicated by bulk rock Sr-Nd-Pb-Hf isotopic signatures (Davies et al., 2006).

From Grubb (1965), a shonknite sill intruding "assumed Tertiary" potassic lavas in North Johor, Malaysia is reported. While data is limited, the Pekan Jabi sill is proposed to have formed via metasomatic processes (Grubb, 1965).

The Eocene Highwood Mountains of Montana, USAare directly east of the AHVF. Here, shonkinites occur with a diverse suite of rocks (e.g. glimmerite, latite, and minette; O'Brien et al., 1991). Highwood shonkinites display major olivine, diopside, biotite, sanidine, and in some samples, nepheline (O'Brien et al., 1991). Here, shonkinites are proposed to have formed from shallow-level fractional crystallization, likely from a combination of enriched lithospheric mantle, asthenospheric mantle, and subduction-related fluids (O'Brien et al., 1991). Nearby is the type locality for shonknites, Shonkin Sag; these rocks display augite, olivine, biotite, and orthoclase as major minerals (Kendrick and Edmond, 1981). Shonkin Sag shonkinites are proposed to have formed as a result of immiscibility where mafic and felsic melts separated to crystallize syenite and shonkinite (Kendrick and Edmond, 1981).

The shonkinites of the Morro de São João (MSJ) pluton, located about 100 km east of Rio de Janeiro are structurally linked with the Neoproterozoic Guanabara Rift, which was reactivated during the separation of Gondwanaland (de Almeida et al., 2000; Brotzu et al., 2007). The MSJ shonkinites occur with nepheline syenites, ultramafic-mafic rocks, alkali syenites, and phonolitic dikes (Brotzu et al., 2007). Valença (1980) suggested that the MSJ evolved via an initial pulse of ultramafic-mafic magmatism followed by more felsic and alkali-rich magmatism. From dating via whole-rock and mineral separates, the MSJ is inferred to have formed between 77 and 56 Ma (Amaral et al., 1967; Sichel et al., 1997). Brotzu et al. (2007) later proposed that the MSJ pluton derived from a phlogopite-bearing, lithosphere-dominated source region as is the case for many of the other Serra do Mar plutons.

Globally, shonkinites occur across a range of tectonic settings from regions of extension associated with continental rifting and supercontinent breakup, to convergent margin tectonics and orogenesis. Shonkinite primary magmas are often associated with heterogeneously metasomatized, lithospheric mantle sources, specifically low degrees of partial melting followed by fractional crystallization, ± crustal assimilation. In rare cases, shonkinite magmas have also been shown to fractionate immiscible carbonate-silicate melts (the Aldan Shield, western Siberia).

Within this global framework, the petrogenesis of the AHVF shonkinites can be evaluated. The first recorded observations of AHVF shonkinites are from Merriwether Lewis on July 16th, 1805, where "a hard black granite" was noted (Corps of Discovery, 1805). Weed and Pirsson (1895) first proposed the term shonkinite after studying the type locality at the nearby Shonkin Sag laccolith. At those locations, Kendrick and Edmond (1981) proposed a magma immiscibility model, in which the laccoliths differentiated in-situ with immiscible alkali-rich mafic and felsic magmas forming as fractional crystallization occurred, leading to an upper laccolith unit of compositionally evolved syenite.

Fig. 13 summarizes the bulk-rock geochemistry available from a global compilation of shonkinite occurrences (discussed above). Some general similarities are observable based on major and minor element oxide compositions. For example, all locales with the exception of the Elchuru alkaline pluton plot within mafic to intermediate alkaline fields on the TAS diagram (Fig. 13a), above the alkaline-subalkaline compositional divide and are high-alkali in nature (as expected) across a relatively restricted range of wt% SiO_2 (~45–55). With the exception of one sample from the Highwood Mountains, all shonkinites are part of the calc-alkaline magma series with a relative lack of FeO enrichment (Fig. 13b).

Fig. 13c shows bulk shonkinite trace elements normalized to primitive mantle. While there is some variation between locales, generally, shonkinites exhibit LILE enrichment and Nb—Ta depletion, a geochemical signature consistent with arc settings. Global shonkinite bulk REE patterns are also generally similar with LREE enrichment, the lack of a prominent Eu anomaly, and relative HREE depletion (Fig. 13d). As shown, the REE abundances of the Mountain Pass shonkinites are consistently elevated which could (in part) be attributed to the subduction of carbonate-bearing sediments ~300 Myrs before the emplacement of the Intrusive Suite, as recently proposed by Benson et al. (2025).

In summary, the global compilation of shonkinite characteristics, including those from the AHVF in this study, indicate that their parental magmas are derived from mantle sources which have previously experienced metasomatism, often in arc-related environments.

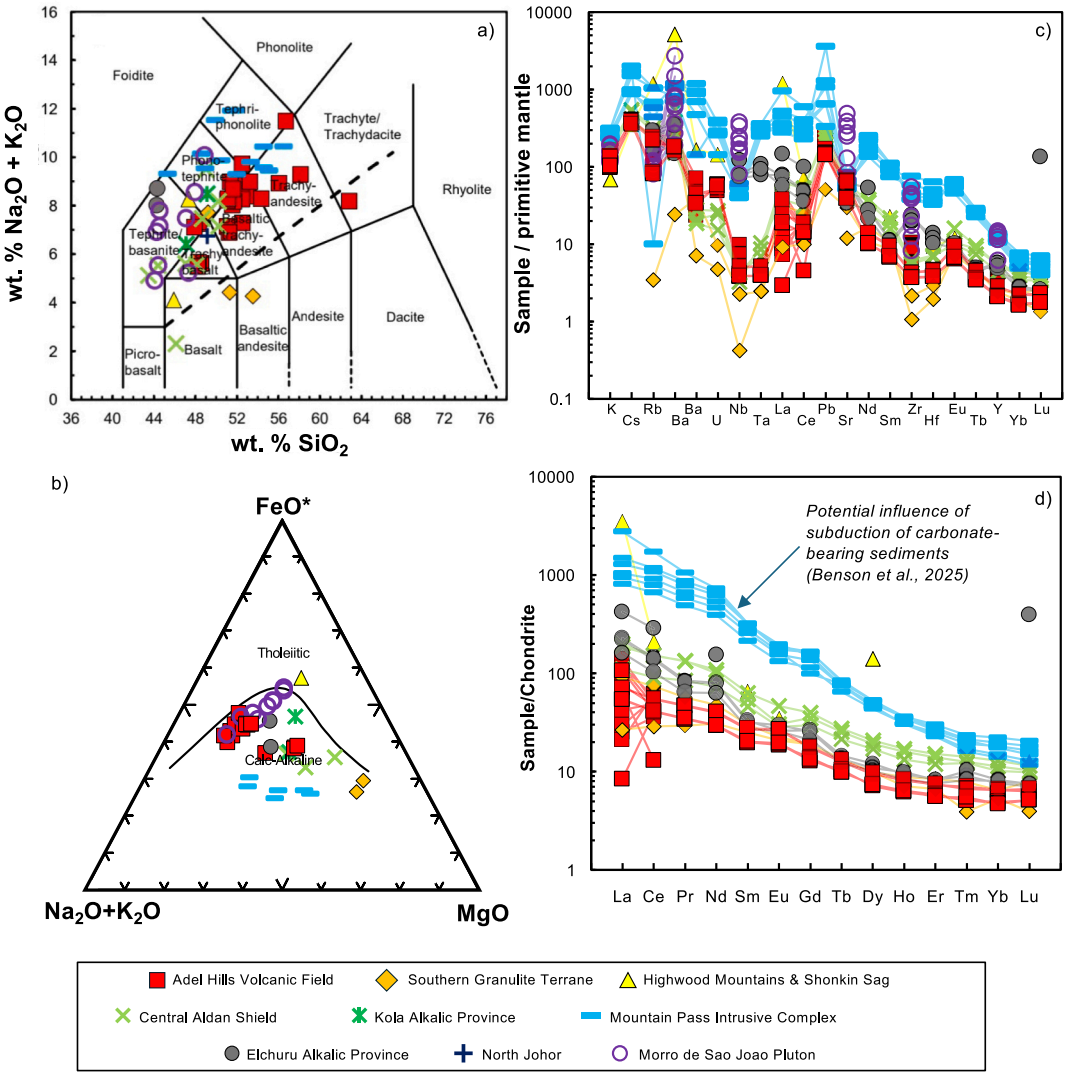

Fig. 13. Comparison diagrams for global shonkinite locales. a) TAS plot after LeBas et al. (1986). b) AFM diagram after Irvine and Baragar (1971). c) Primitive-mantle normalized trace element spidergram (values after Sun and McDonough, 1989). d) Chondrite-normalized REE spidergram (values from Sun and Sun and McDonough, 1989). Data from this study: Grubb (1965); Beall (1973); Kendrick and Edmond (1981); Shadenkov et al. (1990); O'Brien et al. (1991); Madhavan et al. (1992); Saravanan and Ramasamy (1995); Cunningham (1999); Brotzu et al. (2007); Rokosova and Panina (2013); Petrovskii et al. (2014); Bogatikov et al. (2015); He et al. (2015); Poletti et al. (2016); Rokosova et al. (2016); Okrugin et al. (2018); Watts et al. (2021).

5.4. *Tectonomagmatic framework of the AHVF*

Magmatic activity associated with the AHVF is constrained to a ~ 3 Myr period, from 73 Ma to 76 Ma as determined by $^{40}Ar/^{39}Ar$ and K—Ar dates obtained from bulk rock and mineral separates (e.g., biotite, plagioclase; Harlan et al., 2005). The location of the AHVF within the GFTZ, along the margins of the Wyoming craton and the Medicine Hat Block (Fig. 2a), has the potential to provide insights into its unique, highly alkalic chemistry. The Wyoming craton rifted from other Laurentian cratonic blocks *c*. 2.15 Ga and later sutured to the Slave Craton *c*. 1.72 Ga(Kilian et al., 2016). The GFTZ exists partially below Phanerozoic sediments and the Mesoproterozoic Belt Basin (Gifford et al., 2018), although the exact nature of the GFTZ is debated (an intracontinental shear zone vs. a Paleoproterozoic suture; e.g., Boerner et al., 1998; Mueller et al., 2002). Within the GFTZ, ~150 Myrs of orogenic events are recorded, culminating in the Big Sky orogeny *c*. 1.78–1.71 Ga (Mueller et al., 2002; Condit et al., 2015; Ronemus et al., 2022). This event is associated with the Great Falls orogeny at *c*. 1.86 Ga, during which new Paleoproterozoic crust was generated in an arc setting as evidenced by the compositions of juvenile meta supra crustal suites in the Little Belt Mountains, and the reworking of older, preexisting Archean-aged crust (Mueller et al., 2002, 2016; Gifford et al., 2018; Harms and Baldwin, 2023). This subduction-related phase of the Great Falls orogeny is also associated with the closure of an ocean basin *c*. 1.77 Ga between the Medicine Hat Block and the Wyoming Craton (Mogk et al., 1992; Mueller et al., 2002, 2005; Gifford et al., 2014, 2018; O'Sullivan et al., 2021). These ancient periods of orogenesis, juvenile crustal production and reworking, and subduction-related tectonism play a crucial important role in establishing (and contributing to) the composition of the mantle sources which later produced the alkali-rich magmas of central Montana, including the AHVF.

The Central Montana Alkalic Province (CMAP) lies to the east of the AHVF. Greater efforts to understand alkali magma petrogenesis in the CMAP has likely occurred due to the potential for rare metal resource mining and extraction (e.g., Nb and Ta; Montana Bureau of Mines and Geology, 2023). The CMAP consists of a suite of predominantly Late Cretaceous – early Tertiary volcanic and plutonic rocks including dikes, laccoliths, sills, and stocks (Harlan, 2006). During the late Cretaceous into the Eocene, the Wyoming Craton and surrounding regions were impacted by convergent margin tectonics with subduction of the

shallowly dipping Farallon plate leading to magmatism ~1000 km inwards of the continental margin (O'Brien et al., 1991; MacDonald et al., 1992). The high alkali nature of the CMAP has been attributed to the partial melting of a heterogenous, variably metasomatized, subcontinental mantle lithosphere with peak magmatism occurring during the early-middle Eocene (54–45 Ma, Marvin et al., 1980, Chadwick, 1981). Study of these highly-alkalic locales (and their entrained xenoliths), particularly for their isotopic characteristics, provides additional insight into the tectonomagmatic evolution of the lithosphere across this region.

From Dave and Li (2016), a shear wave velocity study revealed a very low shear wave velocity zone underlying the Wyoming craton. This zone was proposed to have formed as a result of Farallon Plate subduction stripping away (in part) the underlying cratonic lithosphere and initiating small-scale convection within the asthenosphere during the Cretaceous. However, metasomatism of the lithospheric mantle may have occurred prior to the onset of Farallon subduction. Study of an ultramafic xenolith suite from the CMAP reported abundant petrographic and geochemical evidence of metasomatism through the presence of veins, enrichment in fluid mobile elements, and depletion in high field strength elements (Downes et al., 2004). Accompanying high $^{87}Sr/^{86}Sr$ ratios were interpreted as indicative of an ancient enrichment event, likely during the mid-Proterozoic (*c*. 1.25 Ga). Along with this xenolith suite, Downes et al. (2004) also investigated a suite of clinopyroxene-rich mica peridotites, also present as xenoliths, in the CMAP. From REE melt equilibration calculations, this suite of ultramafic xenoliths was interpreted to represent a much younger period of lithospheric metasomatism, coincident with Eocene magmatism. In summary, three causes for metasomatism of the lithospheric mantle were proposed by Downes et al. (2004): 1) the formation of clinopyroxenite veins and mica-bearing websterite from silicate melts; 2) phlogopite crystallization from hydrous, K-rich fluids; and 3) development of orthopyroxenite veins, and porphyroblasts of orthopyroxene as a result of mantle interaction with aqueous fluids.

From study of CMAP ultramafic peridotite xenoliths and calculated *Re*-isotope model by Carlson and Irving (1994), older mantle partial melting events beneath the Wyoming Craton at 2.9 Ga (Mesoarchean) and 2.5 Ga (Neoarchean) are proposed. These ages are consistent with late Archean Nd model ages from harzburgite and glimmerite xenoliths, also reported in Carlson and Irving (1994). Throughout other CMAP ultramafic xenolith occurrences, younger isotope model ages are reported (e.g., Re-isotope model ages of 2.5 Ga to 1.7 Ga (Carlson et al., 1999). In addition, monazite and zircon ages from glimmerite veins yield ages *c*. 1.8 Ga (Carlson and Irving, 1994; Rudnick et al., 1999). From Downes et al. (2004), this was interpreted as representing metasomatism of the mantle beneath the Wyoming Craton during the mid-Proterozoic (and consistent with inferences from Sr-isotope data of phlogopite). This may also correlate with the development of the GFTZ. In order to account for the geochemical signatures of the CMAP cumulate xenoliths a model for subduction-induced metasomatism occurring again during the Cretaceous is proposed, which resulted in a high-K, phlogopite-bearing mantle wedge beneath Central Montana.

While the tectonomagmatic conditions under the Wyoming Craton during Farallon Plate subduction led to the partial melting conditions needed to generate a suite of alkali-rich melts and ultimately establish the AHVF during the late Cretaceous, the role of previous mantle metasomatism during continent (re)cycling over several billions of years has likely led to a fertile, hydrous, and geochemically heterogeneous mantle lithosphere at depth.

5.5. Directions for future work

The results of this study could be built on in several ways in order to provide additional insights into the petrogenesis of shonkinites in the AHVF, the magmatic evolution of the AHVF as contractional deformation waned, and to contribute highly alkali magma formation. First, diopside mineral geothermobarometry is recommended in order to constrain the P-T conditions of magma storage within the (likely) shallow lithosphere (e.g., Petrelli et al., 2020). Second, high resolution element maps of multiple diopside crystals should be acquired via EPMA and LA-ICP-MS in order to investigate element partitioning as it relates to the growth of different crystal faces (e.g., Wang et al., 2022). Third, bulk rock Sr-Nd-Pb-Hf-Os isotopes accompanied by in situ LA-MC-ICP-MS analysis of diopsides and apatites for their $^{87}Sr/^{86}Sr$ signatures is recommended in order to constrain the potential contribution from mantle and crustal-derived sources to AHVF magmatism (e.g., Mulder et al., 2023).

6. Conclusions

This study reports the first detailed petrographic, mineralogical, and geochemical investigation of the shonkinite dikes within the AHVF in central Montana. Studied samples are porphyritic (~25–35 %) and characterized by glossy pyroxenes up to 1.1 cm. Shonkinite mineralogy is dominated by clinopyroxene (mostly diopside with minor augite), plagioclase, K-feldspar, and zeolite, along with minor apatite, amphibole, magnetite, and rare calcite. Notably, clinopyroxenes display both sector and oscillatory zoning. Sample analysis via SEM-EDS also revealed rare pyrite. Bulk sample mineralogy via XRD reveals diopside, bytownite, sanidine, analcime, fluorapatite, and magnetite. Bulk rock wt % SiO_2 ranges from 47 to 49 wt%, with total alkalis between 5.50 and 7.34 wt%, consistent with a shonkinite classification. Primitive-mantle normalized bulk trace element signatures reveal LILE enrichment and Nb—Ta depletion and are consistent with a volcanic arc setting. Chondrite-normalized bulk REE signatures reveal significant LREE enrichments: La_N/Sm_N = 2.69–5.38. In-situ mineral analysis via EPMA reveals consistent diopside compositions (n = 100; $Es_{35–42}$,$Fs_{11–17}$, $Wo_{44–49}$) and confirms the presence of plagioclase (predominantly bytownite), alkali feldspar, fluorapatite, and magnetite. High-resolution mapping via EPMA of diopside reveals sector zoning and sub-mm oscillatory zoning. In-situ mineral analysis via LA-ICP-MS of diopsides reveals variable LREE depletion (La_N/Sm_N = 0.47–1.03) and MREE enrichment (Sm_N/Dy_N = 2.30–2.37). LA-ICP-MS of apatites reveals LREE enrichment (La_N/Sm_N = 2.1–2.4; La_N/Lu_N = 21.3–26.7).

Bulk rock trace element systematics are consistent with the AHVF shonkinites being associated with alkali-rich magmas in a volcanic arc system. From high-resolution element mapping, diopside Si, Mg-enrichment is accompanied by Al, Ti, Na, and Cr-depletion on {−111} and relative enrichment in Al, Ti, Na, and Cr is accompanied by depletion in Si and Mg on prism sectors. This is interpreted to result from low degrees of undercooling during crystallization (ΔT = 13-25 °C). The lack of dendritic patterns at the Al sector boundaries further supports this. The trace element chemistries of apatite present in diopsides as inclusions are consistent with crystallization from alkali-rich, mafic melts with geochemical affinities to carbonatite-like compositions. Considering Ce/Ce* vs. Eu/Eu* systematics, apatites are interpreted to have crystallized in a hydrous, oxidizing magmatic environment in which plagioclase crystallization was suppressed. This is supported by the calc-alkaline affinity of the shonkinites and the volcanic arc setting, and also likely accounts for the lack of significant negative Eu anomalies within apatites, clinopyroxenes, and bulk rock signatures.

From a comprehensive review of global shonkinite occurrences, petrogenesis of the AHVF shonkinites is consistent with previous work globally: partial melting of a variably metasomatized, heterogeneous subcontinental mantle lithosphere. For the AHVF in central Montana, this is inferred to have occurred in a contractional tectonomagmatic setting in which a metasomatized arc mantle wedge experienced low degrees of partial melting prior to the collapse of the Cordilleran fold and thrust belt and subsequent lithospheric extension in the middle Eocene-early Miocene.

CRediT authorship contribution statement

C.L. McLeod: Conceptualization, Methodology, Formal analysis, Investigation, Data curation, Writing – review & editing, Visualization, Supervision, Project administration, Funding acquisition. **M.L. Lytle:** Methodology, Validation, Formal analysis, Resources, Data curation, Writing – review & editing, Supervision. **T.J. Cracas:** Methodology, Formal analysis, Investigation, Data curation, Writing – original draft, Writing – review & editing, Visualization. **K.L. Brown:** Methodology, Formal analysis, Data curation, Writing – review & editing. **B.J. Shaulis:** Methodology, Validation, Resources, Data curation, Writing – review & editing. **M. Loocke:** Methodology, Validation, Resources, Data curation, Writing – review & editing.

Declaration of competing interest

The authors declare that they have no known competing financial interests or personal relationships that could have appeared to influence the work reported in this paper.

Acknowledgments

The authors extend thanks to the Miami University's Center for Advanced Microscopy and Imaging (CAMI) and Dr. Zachery Oestreicher for supporting the SEM facilities. Throughout this work, author Cracas was supported by a Graduate Teaching Assistantship from the Department of Geology and Environmental Earth Science at Miami University. Special thanks are extended to Jim and Susan Naus for financial support via the Naus Family Scholar Fund awarded to author McLeod, which supported field work and subsequent data acquisition via EPMA and LA-ICP-MS. The authors are grateful to Teresa Ubide, one anonymous reviewer, and editor Shane Cronin for their insightful and constructive feedback which greatly improved this manuscript.

Appendix A. Supplementary data

Supplementary data to this article can be found online at https://doi.org/10.1016/j.jvolgeores.2025.108496.

Data availability

Data will be made available on request.

References

Amaral, G., Bushee, J., Cordani, U.G., Kawashita, K., Reynolds, J.H., 1967. Potassium-argon ages of alkaline rocks from Southern Brazil. Geochim. Cosmochim. Acta 31, 117–142. https://doi.org/10.1016/S0016-7037(67)80041-3.

Anderson, J.L., Bender, E.E., 1989. Nature and origin of Proterozoic A-type granitic magmatism in the southwestern United States of America. Lithos 23 (1–2), 19–52. https://doi.org/10.1016/0024-4937(89)90021-2.

Anderson, J.R., Payne, J.L., Kelsey, D.E., Hand, M., Collins, A.S., Santosh, M., 2012. High-pressure granulites at the dawn of the Proterozoic. Geology 40 (5), 431–434. https://doi.org/10.1130/G32854.1.

Beall, J.J., 1973. Mechanics of Intrusion and Petrochemical Evolution of the Adel Mountain Volcanics. University of Montana, Missoula unpub. Ph.D dissertation. Available online, accessed 04.04.25: https://scholarworks.umt.edu/etd/9830/.

Bellon, H., Houlgatte, E., Gouronnec, P., Blanchet, R., Tardy, M., Tour Du Pin, H., Vot, M., Villien, A., 1989. Mesozoic and Cenozoic magmatism in the Overthrust Belt (North American Cordilleras, U.S.A.). 40K-40Ar ages and geodynamic significance. Bull. Geol. Soc. France 8, 627–637. https://doi.org/10.2113/gssgfbull.V.3.627.

Belousova, E.A., Griffin, W.L., O'Reilly, S.Y., Fisher, N.I., 2002. Apatite as an indicator mineral for mineral exploration: trace-element compositions and their relationship to host rock type. J. Geochem. Explor. 76 (1), 45–69. https://doi.org/10.1016/S0375-6742(02)00204-2.

Benson, E.K., Watts, K.E., Hillenbrand, I.W., 2025. Geochemistry and radiogenic isotopes constrain the mantle source region of the Mountain Pass Intrusive Suite, California. Lithos 508–509, 108060. https://doi.org/10.1016/j.lithos.2025.108060.

Boerner, D.E., Craven, J.A., Kurtz, R.D., Ross, G.M., Jones, F.W., 1998. The Great Falls Tectonic Zone: suture or intracontinental shear zone? Can. J. Earth Sci. 35, 175–183. https://doi.org/10.1139/e97-104.

Bogatikov, O.A., Kononova, V.A., Pervov, V.A., Zhuravlev, D.A., 1994. Petrogenesis of mesozoic potassic magmatism of the Central Aldan: a Sr-Nd isotopic and geodynamic model. Int. Geol. Rev. 36 (7), 629–644. https://doi.org/10.1080/00206819409465479.

Boraiaha, C.K., Joshi, K.B., Kerr, A.C., Padhi, J.K., Mishra, S.S., Chandan, R., 2020. Field, petrographic and geochemical characteristics of Sullya alkaline complex in the Cauvery Shear Zone (CSZ), southern India: implications for petrogenesis. J. Earth Sci. Syst. 129 (111). https://doi.org/10.1007/s12040-020-1369-1.

Bowen, N.L., 1922. The behavior of inclusions in igneous magmas. J. Geol. v, 30. https://www.journals.uchicago.edu/doi/abs/10.1086/622928.

Bowen, N.L., 1928. The Evolution of the Igneous Rocks. Princeton University Press.

Bowen, N.L., 1945. Phase equilibria bearing on the origin a differentiation of alkaline rocks. Am. J. Sci. 243, 75–89.

Bowring, S.A., Housh, T., 1995. The Earth's early evolution. Science 269 (5230), 1535–1540. https://doi.org/10.1126/science.7667634.

Bromiley, G.D., 2021. Do concentrations of Mn, Eu and Ce in apatite reliably record oxygen fugacity in magmas? Lithos 384, 105900. https://doi.org/10.1016/j.lithos.2020.105900.

Brotzu, P., Melluso, L., Gomes, C.B., Lustrino, M., Morbidelli, L., Morra, V., Ruberti, E., Tassinari, C., D'Antonio, M., 2007. Petrogenesis of the Early Cenozoic potassic alkaline complex of Morro de São João, southeastern Brazil. J. South Am. Earth Sci. 24 (1), 93–115. https://doi.org/10.1016/j.jsames.2007.02.006.

Bruand, E., Fowler, M., Stoery, C., Laurent, O., Antoine, C., Guitreau, M., Heilmo, E., Nebel, O., 2020. Accessory mineral constraints on crustal evolution: elemental fingerprints for magma discrimination. Geochem. Perspect. Lett. 13, 17–22. https://doi.org/10.7185/geochemlet.2006.

Burns, D.H., de Silva, S.L., 2023. Andesites and evolution of the continental crust: perspectives from the Central Volcanic Zone of the Andes. Front. Earth Sci. https://doi.org/10.3389/feart.2022.961130.

Carlson, R.W., Irving, A.J., 1994. Depletion and enrichment history of subcontinental lithospheric mantle: an Os, Sr, Nd and Pb isotopic study of ultramafic xenoliths from the northwestern Wyoming Craton. Earth Planet. Sci. Lett. 126 (4), 457–472. https://doi.org/10.1016/0012-821X(94)90124-4.

Carlson, R.W., Irving, A.J., Hearn Jr., B.C., 1999. Chemical and isotopic systematics of peridotite xenoliths from the Williams kimberlite, Montana: clues to processes of lithosphere formation, modification and destruction. In: Gurney, J.J., Gurney, J.L., Pascoe, M.D., Richardson, S.H. (Eds.), Proceedings of the VIIth International Kimberlite Conference, v. 1. Cape Town, pp. 90–98.

Castor, S.B., 2008. The mountain pass rare-Earth carbonatite and associated ultrapotassic rocks, California. Can. Mineral. 46 (4), 779–806. https://doi.org/10.3749/canmin.46.4.779.

Chadwick, R.A., 1981. Chronology and structural setting of volcanism in Southwestern and Central Montana. In: Montana Geological Society Field Conference and Symposium Guidebook to Southwest Montana, pp. 141–148.

Chandler, R., Bhat, G., Mavrogenes, J., Knell, B., David, R., Leggo, T., 2024. The primary geology of the Paleoproterozoic Mt Weld Carbonatite Complex, Western Australia. J. Petrol. 65 (2). https://doi.org/10.1093/petrology/egae007.

Chen, J.-L., Xu, J.-F., Wang, B.-D., Kang, Z.-Q., Jie, L., 2010. Origin of Cenozoic alkaline potassic volcanic rocks at KonglongXiang, Lhasa terrane, Tibetan Plateau: products of partial melting of a mafic lower-crustal source? Chem. Geol. 273, 286–299. https://doi.org/10.1016/j.chemgeo.2010.03.003.

Chen, L., Zheng, Y.-F., Zhao, Z.-F., 2018. Geochemical insights from clinopyroxene phenocrysts into the effect of magmatic processes on petrogenesis of intermediate volcanics. Lithos 316-317, 137–153. https://doi.org/10.1016/j.lithos.2018.07.014.

Chen, K., Tang, M., Hu, Z., Liu, Y., 2023. Generation of tholeiitic and calc-alkaline arc magmas and its implications for continental growth. Geochim. Cosmochim. Acta 335, 173–183. https://doi.org/10.1016/j.gca.2023.07.002.

Condit, C.B., Mahan, K.H., Ault, A.K., Flowers, R.M., 2015. Foreland-directed propagation of high-grade tectonism in the deep roots of a Paleoproterozoic collisional orogen, SW Montana, USA. Lithosphere 7 (6), 625–645. https://doi.org/10.1130/L460.1.

Cook, N.J., Ciobanu, C.L., Wade, B.P., Gilbert, S.E., Alford, R., 2023. Mineralogy and distribution of REE in oxidised ores of the Mount Weld Laterite Deposit, Western Australia. Minerals 13 (656). https://doi.org/10.3390/min13050656.

Corps of Discovery, 1805. July 16th, 1805, As Collected by the Journals of the Lewis and Clark Expedition Online Archive: University of Nebraska-Lincoln. https://lewisandclarkjournals.unl.edu/item/lc.jrn.1805-07-16.

Costa, F., Shea, T., Ubide, T., 2020. Diffusion chronometry and the timescales of magmatic processes. Nat. Rev. Earth Environ. 1, 201–214. https://doi.org/10.1038/s43017-020-0038-x.

Cruz-Uribe, A.M., Marschall, H.R., Gaetani, G.A., Le Roux, V., 2018. Generation of alkaline magmas in subduction zones by partial melting of mélange diapirs - an experimental study. Geology 46 (4), 343–346. https://doi.org/10.1130/G39956.1.

Cunningham, B.L., 1999. Petrogenesis of the Adel Mountains Volcanic Field, Central Montana. University of Montana, Missoula unpub. Master's thesis. Available online, accessed 04.04.25: https://scholarworks.umt.edu/etd/7507/.

Daly, R.A., 1914. Igneous Rocks and Their Origin. McGraw-Hill Book Company, Inc, New York.

Dave, R., Li, A., 2016. Destruction of the Wyoming craton: Seismic evidence and geodynamic processes. Geology 44 (11), 883–886. https://doi.org/10.1130/G38147.1.

Davies, G.R., Stolz, A.J., Mahotkin, I.L., Nowell, G.M., Pearson, D.G., 2006. Trace element and Sr–Pb–Nd–Hf isotope evidence for ancient, fluid-dominated enrichment of the source of Aldan Shield Lamproites. J. Petrol. 47 (6), 1119–1146. https://doi.org/10.1093/petrology/egl005.

de Almeida, F.F.M., de Brito Neves, B.B., Carneiro, C.D.R., 2000. The origin and evolution of the South American Platform. Earth Sci. Rev. 50 (1–2), 77–111. https://doi.org/10.1016/S0012-8252(99)00072-0.

Denton, K.M., Ponce, D.A., Peacock, J.R., Miller, D.M., 2020. Geophysical characterization of a Proterozoic REE terrane at Mountain Pass, eastern Mojave Desert, California, USA. Geosphere 16 (1), 456–471. https://doi.org/10.1130/GES02066.1.

Downes, H., MacDonald, R., Upton, B.J., Cox, K.G., Bodiner, J.-L., Mason, P.R.D., James, D., Hill, P.G., Hearn Jr., B.C., 2004. Ultramafic xenoliths from the Bearpaw Mountains, Montana, USA: evidence for multiple metasomatic events in the lithospheric mantle beneath the Wyoming Craton. J. Petrol. 45 (8), 1631–1662. https://doi.org/10.1093/petrology/egh027.

Dowty, E., 1976. Crystal structure and crystal growth: II. Sector zoning in minerals. Am. Mineral. 61, 460–469.

Foley, S.F., Fischer, T.P., 2017. An essential role for continental rifts and lithosphere in the deep carbon cycle. Nat. Geosci. 10, 897–902. https://doi.org/10.1038/s41561-017-0002-7.

Fuentes, F., DeCelles, P., Constenius, K.N., 2012. Regional structure and kinematic history of the Cordilleran fold-thrust belt in northwestern Montana, USA. Geosphere 8 (5), 1104–1138. https://doi.org/10.1130/GES00773.1.

Gadea, O.C.A., Khan, S.D., Sisson, V.B., 2024. Estimating rare earth elements at various scales with bastnäsite indices for Mountain Pass. Ore Geol. Rev. 173. https://doi.org/10.1016/j.oregeorev.2024.106254.

Ghodke, S.S., Rathana, K., Kokandakar, G.J., Nagaraju, B., More, L.B., Bholse, M.V., Kumar, K.V., 2018. Emplacement and growth of alkaline dikes: Insights from the shonkinite dikes (Elchuru alkaline complex, SE India). J. Struct. Geol. 117, 219–236. https://doi.org/10.1016/j.jsg.2018.09.016.

Gifford, J.N., Mueller, P.A., Foster, D.A., Mogk, D.W., 2014. Precambrian crustal evolution in the great falls tectonic zone: insights from xenoliths from the Montana Alkali Province. J. Geol. 122, 531–548. https://doi.org/10.1086/677262.

Gifford, J.N., Mueller, P.A., Foster, D.A., Mogk, D.W., 2018. Extending the realm of Archean crust in the Great Falls tectonic zone: evidence from the Little Rocky Mountains, Montana. Precambrian Res. 315, 264–281. https://doi.org/10.1016/j.precamres.2018.07.021.

Grove, T.L., Brown, S.M., 2018. Magmatic processes leading to compositional diversity in igneous rocks: Bowen (1928) revisited. Am. J. Sci. 318, 1–28. https://doi.org/10.2475/01.2018.02.

Grubb, P.L.C., 1965. Undersaturated Potassic Lavas and Hypabyssal Intrusives in North Johore. Geology 102 (4).

Gunderson, J.A., Sheriff, S.D., 1991. A new Late Cretaceous paleomagnetic pole from the Adel Mountains, West Central Montana. J. Geophys. Res. 96, 317–326. https://doi.org/10.1029/90JB01963.

Hanson, G.N., 1980. Rare earth elements in petrogenetic studies of igneous systems. Annu. Rev. Earth Planet. Sci. 8, 371–406. https://doi.org/10.1146/annurev.ea.08.050180.002103.

Harlan, S.S., 2006. 40Ar/39Ar dates from alkaline intrusions in the northern Crazy Mountains, Montana: Implications for the timing and duration of alkaline magmatism in the Central Montana alkalic province. Rocky Mountain. Geology 41 (1), 45–55. https://doi.org/10.2113/gsrocky.41.1.45.

Harlan, S.S., Snee, L.W., Reynolds, M.W., Mehnert, H.H., Schmidt, R.G., Sheriff, S.D., Irving, A.J., 2005. 40Ar/39Ar geochronology and tectonic significance of the Upper Cretaceous Adel Mountain Volcanics and spatially associated Tertiary igneous rocks, northwestern Montana: Reston. In: US Geological Survey Professional Paper 1696. https://doi.org/10.3133/pp1696.

Harlan, S.S., Geissman, J.W., Whisner, S.C., Schmidt, C.J., 2008. Paleomagnetism and geochronology of sills of the Doherty Mountain area, southwestern Montana: Implications for the timing of fold-and-thrust belt deformation and vertical-axis rotations along the southern margin of the Helena salient. GSA Bull. 120 (9–10), 1091–1104. https://doi.org/10.1130/B26313.1.

Harms, T.A., Baldwin, J.A., 2023. Paleoproterozoic geology of SW Montana: implications for the paleogeography of the Wyoming craton and for the consolidation of Laurentia. In: Whitmeyer, S.J., Williams, M.L., Kellett, D.A., Tikoff, B. (Eds.), GSA Memoirs Laurentia: Turning Points in the Evolution of a Continent, p. 804. https://doi.org/10.1130/2022.1220(05).

He, X.-F., Santosh, M., Zhang, Z.-M., Tsunogae, T., Chetty, T.R.K., Mohan, M.R., Anbazhagan, S., 2015. Shonkinites from Salem, southern India: Implications for Cryogenian alkaline magmatism in rift-related setting. J. Asian Earth Sci. 113, 812–825. https://doi.org/10.1016/j.jseaes.2015.07.002.

He, X.-F., Santosh, M., Tsunogae, T., Malaviarachchi, S.P.K., Dharmapriya, P.L., 2016. Neoproterozoic arc accretion along the 'eastern suture' in Sri Lanka during Gondwana assembly. Precambrian Res. 279, 57–80. https://doi.org/10.1016/j.precamres.2016.04.006.

He, X.-F., Hand, M., Santosh, M., Kelse, D.E., Morissey, L.J., Tsunogae, T., 2018. Long-lived metamorphic P–T–t evolution of the Highland Complex, Sri Lanka: Insights from mafic granulites. Precambrian Res. 316, 227–243. https://doi.org/10.1016/j.precamres.2018.08.008.

Hellstrom, J., Paton, C., Woodhead, J., Hergt, J., 2008. Iolite: software for spatially resolved LA-(quad and MC) ICPMS analysis. Mineral. Assoc. Canada Short Course Ser. 40, 343–348.

Herring, C., 1951. Some theorems on the free energies of crystal surfaces. Phys. Rev. J. 82, 87–93. https://doi.org/10.1103/PhysRev.82.87.

Holmes, A., 1932. The origin of igneous rocks. Geol. Mag. 69 (12), 543–558. https://doi.org/10.1017/S0016756800098332.

Howlett, C.J., Jepson, G., Carrapa, B., DeCelles, P.G., Constentius., K.N., 2024. Late cretaceous exhumation of the Little Belt Mountains and regional development of the Helena salient, west-Central Montana, USA. GSA Bulletin 136 (5–6), 2256–2280. https://doi.org/10.1130/B37081.1.

Hyndman, D.W., Alt, D., 1987. Radial dikes, laccoliths, and gelatin models. J. Geol. 95, 763–774.

Irvine, T.N., Baragar, W.R.A., 1971. A guide to the chemical classification of the common volcanic rocks. Can. J. Earth Sci. 8 (5). https://doi.org/10.1139/e71-055.

Jagoutz, O., 2014. Arc crustal differentiation mechanisms. Earth Planet. Sci. Lett. 396, 267–277. https://doi.org/10.1016/j.epsl.2014.03.060.

Jochum, K.P., Weis, U., Stoll, B., Kuzmin, D., Yang, Q., Raczek, I., Jacob, D.E., Stracke, A., Birbaum, K., Frick, D.A., Günther, D., Enzweiler, J., 2011. Determination of reference values for NIST SRM 610–617 glasses following ISO guidelines. Geostand. Geoanal. Res. 35 (4), 397–429. https://doi.org/10.1111/j.1751-908X.2011.00120.x.

Kauffman, E.G., Caldwell, W.E., 1993. The western interior basin in space and time. In: Caldwell, W.E., Kauffman, E.G. (Eds.), Evolution of the Western Interior Basin. Special. Papers of the Geological, 39. Association of Canada, pp. 1–30.

Kendrick, G.C., Edmond, C.L., 1981. Magma Immiscibility in the Shonkin Sag and Square Butte Laccoliths: Missoula. University of Montana. https://doi.org/10.1130/0091-7613(1981)9%3C615:MIITSS%3E2.0.CO;2.

Ketcham, R.A., 2015. Technical note: Calculation of stoichiometry from EMP data for apatite and other phases with mixing on monovalent anion sites. Am. Mineral. 100 (7), 1620–1623. https://doi.org/10.2138/am-2015-5171.

Khan, M., Li, H., Algeo, T.J., Khan, A., Khan, A., Xie, Y., 2025. Apatite as an indicator of tectono-magmatic evolution of silica-undersaturated to silica-oversaturated rocks on the NW Indian Plate margin. Chem. Geol. 672, 122516. https://doi.org/10.1016/j.chemgeo.2024.122516.

Kharkongor, M.B.K., Glorie, S., Mulder, J., Kirkland, C.L., Chew, D., Kohn, B., Simpson, A., 2023. Apatite laser ablation Lu–Hf geochronology: a new tool to date mafic rocks. Chem. Geol. 636. https://doi.org/10.1016/j.chemgeo.2023.121630.

Kieffer, M.A., Dare, S.A.S., Namur, O., 2023. The use of trace elements in apatite to trace differentiation of a ferrobasaltic melt in the Sept-Iles Intrusive Suite, Quebec, Canada: Implications for provenance discrimination. Geochimica et Cosmochimia Acta 342, 169–197. https://doi.org/10.1016/j.gca.2022.12.016.

Kieffer, M.A., Dare, S.A.S., Gendron, M., 2024a. Trace element discrimination diagrams to identify igneous apatite from I-, S- and A-type granites and mafic intrusions: Implications for provenance studies and mineral exploration. Chem. Geol. 649. https://doi.org/10.1016/j.chemgeo.2024.121965.

Kieffer, M.A., Dare, S.A.S., Namur, O., Mansur, E.T., 2024b. Apatite chemistry as a petrogenetic indicator for mafic layered intrusions. J. Petrol. 65 (4), egae022. https://doi.org/10.1093/petrology/egae022.

Kilian, T.M., Chamberlain, K.R., Evans, D.A.D., Bleeker, W., Cousens, B.L., 2016. Wyoming on the run–toward final Paleoproterozoic assembly of Laurentia. Geology 44 (10), 863–866. https://doi.org/10.1130/G38042.1.

Kirkpatrick, R.J., Kuo, L.-C., Melchior, J., 1981. Crystal growth in incongruently-melting compositions: programmed cooling experiments with diopside. Am. Mineral. 66 (3–4), 223–241.

Klassy, T., 2024. The Shonkin Sag: One of the Most Important Geological Sites in the World. Available online, accessed 04.05.25. https://www.distinctlymontana.com/shonkin-sag-one-most-important-geological-sites-world.

Kochetkov, A.Ya., 2006. Mesozoic gold-bearing ore-magmatic systems of Central Aldan. Russian Geol. Geophys. 47 (7), 847–861.

Kouchi, A., Sugawara, Y., Kashima, K., Sunagawa, I., 1983. Laboratory growth of sector zoned clinopyroxenes in the system CaMgSi2O6-CaTiAl2O6. Contrib. Mineral. Petrol. 83, 177–184. https://link.springer.com/article/10.1007/BF00373091.

LeBas, M.J., Lemaitre, R.W., Streckeisen, A., Zenettin, B., 1986. A chemical classification of volcanic rocks based on the total alkali silica diagram. J. Petrol. 27 (3), 745–750. https://doi.org/10.1093/petrology/27.3.745.

Lyons, J.B., 1944. Igneous rocks of the northern big Belt Range, Montana. Bull. Geol. Soc. Am. 55, 445–472. https://doi.org/10.1130/GSAB-55-445.

MacDonald, R., Upton, B.G.J., Collerson, K.D., Hearn, B.C., James, D., 1992. Potassic Mafic Lavas of the Bearpaw Mountains, Montana: Mineralogy, Chemistry, and Origin. J. Petrol. 33, 305–346. https://doi.org/10.1093/petrology/33.2.305.

MacDonald, A., Ubide, T., Mollo, S., Masotta, M., Pontesilli, A., 2022. Trace element partitioning in zoned clinopyroxene as a proxy for undercooling: Experimental constraints from trachybasaltic magmas. Geochim. Cosmochim. Acta 336, 249–268. https://doi.org/10.1016/j.gca.2022.09.007.

MacDonald, A., Ubide, T., Mollo, S., Pontesilli, A., Masotta, M., 2023. The influence of undercooling and sector zoning on clinopyroxene–melt equilibrium and thermobarometry. J. Petrol. 64, 1–18. https://doi.org/10.1093/petrology/egad074.

MacDonald, A., Ubide, T., Mollo, S., 2024. Degree of sector zoning in clinopyroxene records dynamic magma recharge and ascent. Geochim. Cosmochim. Acta 378, 245–258. https://doi.org/10.1016/j.gca.2024.06.025.

Madhavan, V., Rao, J.M., Balaram, V., Kumar, R., 1992. Geochemistry and petrogenesis of lamprophyres and associated dykes from Elchuru, Andhra Pradesh, India. J. Geol. Soc. India 40, 135–149. https://doi.org/10.17491/jgsi/1992/400205.

Maruyama, G., Hiraga, T., 2017. Grain- to multiple-grain-scale deformation processes during diffusion creep of forsterite + diopside aggregate: 2. Grain boundary sliding-induced grain rotation and its role in crystallographic preferred orientation in rocks. J. Geophys. Res. Solid Earth 122, 5916–5934. https://doi.org/10.1002/2017JB014255.

Marvin, R.F., Hearn, B.C., Mehnert, H.H., Naeser, C.W., Zartman, R.E., Lindsey, D.A., 1980. Late Cretaceous-Paleocene-Eocene igneous activity in north-central Montana. Bull. Isotop. Geochronol. 29. Available online, accessed 04.05.25;. https://geoinfo.nmt.edu/publications/periodicals/isochronwest/29/iw_v29_p05.pdf.

Masotta, M., Pontesilli, A., Mollo, S., Armienti, P., Ubide, T., Nazzari, M., Scarlato, P., 2020. The role of undercooling during clinopyroxene growth in trachybasaltic

magmas: insights on magma decompression and cooling at Mt. Etna volcano. Geochim. Cosmochim. Aca 268, 258–276. https://doi.org/10.1016/j.gca.2019.10.009.
McCubbin, F.M., Joliff, B.J., Nekvasil, H., Carpenter, P.K., Zeigler, R.A., Steele, A., Elardo, S.M., Lindsley, D.H., 2011. Fluorine and chlorine abundances in lunar apatite: Implications for heterogeneous distributions of magmatic volatiles in the lunar interior. Geochim. Cosmochim. Acta 75 (17), 5073–5093. https://doi.org/10.1016/j.gca.2011.06.017.
Mikhailova, J.A., Ivanyuk, G.Y., Kalashnikov, A.O., Pakhomovsky, Y.A., Bazai, A.V., Yakovenchuck, V.N., 2019. Petrogenesis of the eudialyte complex of the Lovozero Alkaline Massif (Kola Peninsula, Russia). Minerals 9 (10), 581. https://doi.org/10.3390/min9100581.
Miles, A.J., Graham, C.M., Hawkesworth, C.J., Gillespie, M.R., Hinton, R.W., Bromiley, G.D., 2014. Apatite: a new redox proxy for silicic magmas? Geochim. Cosmochim. Acta 132, 101–119. https://doi.org/10.1016/j.gca.2014.01.040.
Mogk, D.W., Mueller, P.A., Wooden, J.L., 1992. The nature of Archean terrane boundaries: an example from the northern Wyoming Province. Precambrian Res. 55 (1–4), 155–168. https://doi.org/10.1016/0301-9268(92)90020-O.
Mollo, S., Hammer, J.E., 2017. Dynamic crystallization in magmas. In: Mineral Reaction Kinematics: Microstructures, Textures, Chemical and Isotopic Signatures, 16. European Mineralogical Society and Mineralogical Society of Great Britain and Ireland. https://doi.org/10.1180/EMU-notes.16.12.
Mollo, S., Del Gaudio, P., Ventura, G., Iezzi, G., Scarlato, P., 2010. Dependence of clinopyroxene composition on cooling rate in basaltic magmas: implications for thermobarometry. Lithos 118 (304), 302–312. https://doi.org/10.1016/j.lithos.2010.05.006.
Mollo, S., Blundy, J., Scarlato, P., Pia De Christofaro, S., Tecciato, V., Di Stefano, F., Vetere, F., Holtz, F., Bachmann, O., 2018. An integrated P-T-H2O-lattice strain model to quantify the role of clinopyroxene fractionation on REE+Y and HFSE patterns of mafic alkaline magmas: application to eruptions at Mt. Etna. Earth Sci. Rev. 185, 32–56. https://doi.org/10.1016/j.earscirev.2018.05.014.
Montana Bureau of Mines and Geology, 2023. Potential Sources of Critical Mineral Commodities in Montana. Available online, accessed 03.24.25. https://archive.legmt.gov/content/Committees/Interim/2023-2024/Environmental-Quality-Council/EQC_Meetings/2023_Sep_28/MBMG-REEs-Oct2023.pdf.
Mudge, M.R., 1970. Origin of the Disturbed Belt in Northwestern Montana. Geol. Soc. Am. Bull. 81, 377–392. https://doi.org/10.1130/0016-7606(1970)81[377:OOTDBI]2.0.CO;2.
Mueller, P.A., Heatherington, A.L., Kelly, D.M., Wooden, J.L., Mogk, D.L., 2002. Paleoproterozoic crust within the Great Falls tectonic zone: implications for the assembly of southern Laurentia. Geology 30 (2), 127–130. https://doi.org/10.1130/0091-7613(2002)030%3C0127:PCWTGF%3E2.0.CO;2.
Mueller, P.A., Burger, H.R., Wooden, J.L., Brady, J.B., Cheney, J.T., Harms, T.A., Heatherington, A.L., Mogk, D.W., 2005. Paleoproterozoic metamorphism in the Northern Wyoming Province: implications for the assembly of Laurentia. J. Geol. 113 (2). https://doi.org/10.1086/427667.
Mueller, P.A., Mogk, D., Wooden, J., Spake, D., 2016. U-Pb ages of zircons from the Lower Belt Supergroup and proximal crystalline basement: Implications for the early evolution of the Belt Basin. In: MacLean, J.S., Sears, J.W. (Eds.), Belt Basin: Window to Mesoproterozoic Earth. https://doi.org/10.1130/2016.2522(11).
Mulder, J., Hagen-Peter, G., Ubide, T., Andreasen, R., Kooijman, E., Kielman-Schmitt, M., Feng, Y.-X., Paul, B., Karlsson, A., Tegner, C., Lesher, C., Costa, F., 2023. New reference materials, analytical procedures and data reduction strategies for sr isotope measurements in geological materials by LA-MC-ICP-MS. Geostand. Geoanal. Res. 47 (2), 311–336. https://doi.org/10.1111/ggr.12480.
Nakamura, E., Campbell, I.H., Sun, S.-S., 1985. The influence of subduction processes on the geochemistry of Japanese alkaline basalts. Nature 316, 55–58. https://doi.org/10.1038/316055a0.
Navarrete, C., Gianni, G., Massaferro, G., Butler, K., 2020. The fate of the Farallon slab beneath Patagonia and its links to Cenozoic intraplate magmatism, marine transgressions and topographic uplift. Earth Sci. Rev. 210. https://doi.org/10.1016/j.earscirev.2020.103379.
Neave, D.A., Putirka, K.D., 2017. A new clinopyroxene-liquid barometer, and implications for magma storage pressures under Icelandic rift zones. Am. Mineral. 102 (4), 777–794. https://doi.org/10.2138/am-2017-5968.
Neuendorf, K.K.E., Mehl, J.P., Jackson, J.A., 2005. Glossary of Geology. American Geological Institute, p. 779.
Ni, H., Keppler, H., Walte, N., Schiavi, F., Chen, Y., Masotta, M., Li, Z., 2014. In situ observation of crystal growth in a basalt melt and the development of crystal size distribution in igneous rocks. Contrib. Mineral. Petrol. 167 (1003). https://doi.org/10.1007/s00410-014-1003-9.
O'Brien, H.E., Irving, A.J., McCallum, S., 1991. Eocene potassic magmatism in the highwood mountains, montana: petrology, geochemistry, and tectonic implications. J. Geophys. Res. 96 (B8), 13237–13260. https://doi.org/10.1029/91JB00599.
Ohnenstetter, D., Brown, W.L., 1992. Overgrowth textures, disequilibrium zoning, and cooling history of a glassy four-pyroxene Boninite Dyke from New Caledonia. J. Petrol. 33 (1), 231–271. https://doi.org/10.1093/petrology/33.1.231.
Okrugin, A.V., Borisenko, A.S., Zhuravlev, A.I., Travin, A.V., 2018. Mineralogical, geochemical, and age characteristics of the rocks of the Inaglidunite–clinopyroxenite–shonkinite massif with platinum–chromite and Cr-diopside mineralization (Aldan Shield). Russian Geol. Geophys. 59. https://doi.org/10.1016/j.rgg.2018.09.008.
Orlova, M.P., 1987. Recent findings on the geology of the MalyyMurun alkalic pluton (southwestern Yakutia). Sovetskayageologiya 30 (9), 945–954 no. 9; 82-83, translated in International Geology Review.
O'Sullivan, G., Chew, D., Kenny, G., Henrichs, I., Mulligan, D., 2020. The trace element composition of apatite and its application to detrital provenance studies. Earth Sci. Rev. 201. https://doi.org/10.1016/j.earscirev.2019.103044.
O'Sullivan, G.J., Thakurdin, Y., Bolhar, R., Horváth, P., Hoare, B.C., Collerson, K.D., 2021. The Great Falls Tectonic Zone after the assembly of Laurentia: evidence for long-term tectonic stability from xenolith apatite. Lithos 384-385, 105977. https://doi.org/10.1016/j.lithos.2021.105977.
Parker, S.D., Pearson, D.M., 2023. A kinematic model linking the Sevier and Laramide belts in the Idaho-Montana fold-thrust belt, U.S. Cordillera. Geosphere 19 (6), 1565–1588. https://doi.org/10.1130/GES02649.1.
Paton, C., Hellstrom, J., Paul, B., Woodhead, J., Hergt, J., 2011. Iolite: freeware for the visualisation and processing of mass spectrometric data. J. Anal. At. Spectrom 26 (12), 2508–2518. https://doi.org/10.1039/C1JA10172B.
Pedersen, J.M., Ulrich, T., Whitehouse, M.J., Kent, A.J.R., Tenger, C., 2021. The volatile and trace element composition of apatite in the Skaergaard intrusion, East Greenland. Contrib. Mineral. Petrol. 176, 102. https://link.springer.com/article/10.1007/s00410-021-01861-x.
Petrelli, M., Caricchi, L., Perugini, D., 2020. Machine learning thermo-barometry: application to clinopyroxene-bearing magmas. J. Geophys. Res. 125 (9), e2020JB020130. https://doi.org/10.1029/2020JB020130.
Petrovskii, M.N., Bayanova, T.B., Petrovskaya, L.S., Bazai, A.V., 2014. Mesoproterozoic peridotite-shonkinite series: a new type of intraplate magmatism in the Kola Alkalic Province. Dokl. Earth Sci. v, 457 part 2. https://doi.org/10.1134/S1028334X14060282.
Philpotts, A., Ague, J., 2009. Principles of Igneous and Metamorphic Petrology. Cambridge University Press. https://doi.org/10.1017/CBO9780511813429. ISBN: 9780511813429.
Poletti, J.E., Cottle, J.M., Hagen-Peter, G.A., Lackey, J.S., 2016. Petrochronological constraints on the origin of the Mountain Pass ultrapotassic and carbonatite intrusive suite, California. J. Petrol. 57 (8). https://doi.org/10.1093/petrology/egw050.
Pollington, A.D., Baxter, E.F., 2011. High precision microsampling and preparation of zoned garnet porphyroblasts for Sm–Nd geochronology. Chem. Geol. 281, 270–282. https://doi.org/10.1016/j.chemgeo.2010.12.014.
Putirka, K.D., 2017. Down the crater: where magmas are stored and why they erupt. Elements 13 (1), 11–16. https://doi.org/10.2113/gselements.13.1.11.
Qu, Y., Liu, X., Liu, X., Huang, Q., Yang, Q., Hu, R., Liu, P., Song, Y., 2024. Petrogenesis and tectonic setting of the proto-tethyandachaidan ophiolite, North China: insights from clinopyroxene chemistry and whole-rock Sr–Nd–Pb and zircon Hf isotopes. Front. Earth Sci. 12. https://doi.org/10.3389/feart.2024.1473101.
Rakhimov, I.R., 2024. Apatite in Pegmatoid Gabbro (Khudolaz differentiated Complex, Southern Urals): electron-microprobe and LA-ICP-MS geochemical study in context of petrogenesis. Minerals 14 (12), 1271. https://doi.org/10.3390/min14121271.
Rakhimov, I.R., Gottman, I.A., Kholodnov, V.V., Chervyakovskiy, V.S., 2022. Geochemistry of accessory apatite from the Cu–Ni–sulfidebearing ultramafic–mafic rocks of the khudolaz complex (South Urals) as a monitor of magmatic and metasomatic processes. Russian Geol. Geophys. 63, 1388–1406. https://doi.org/10.2113/RGG20214423.
Renjith, M.L., Charan, S.N., Subbarao, D.V., Babu, E.V.S.S.K., Rajashekhar, V.B., 2014. Grain to outcrop-scale frozen moments of dynamic magma mixing in the syenite magma chamber, Yelagiri Alkaline Complex, South India. Geosci. Front. 5 (6), 801–820. https://doi.org/10.1016/j.gsf.2013.08.006.
Rokosova, E.Yu., Panina, L.I., 2013. Shonkinites and minettes of the Ryabinovyi massif (Central Aldan): composition and crystallization conditions. Russian Geol. Geophys. 54, 613–626. https://doi.org/10.1016/j.rgg.2013.04.011.
Rokosova, E.Yu., Panina, L.I., Vasil'ev, Yu.R, Lesnov, F.P., 2016. Conditions of crystallization of olivine shonkinites in the Inglai massif (Central Aldan). Russ. Geol. Geophys. 57, 1298–1311. https://doi.org/10.1016/j.rgg.2016.08.015.
Ronemus, C.B., Orme, D.A., Guenthner, W.R., Cox, S.E., Kussmaul, C.A.L., 2022. Orogens of big sky country: reconstructing the deep-time tectonothermal history of the Beartooth Mountains, Montana and Wyoming, USA. Tectonics 42 (1), e2022TC007541. https://doi.org/10.1029/2022TC007541.
Rudnick, R.I., Ireland, T.R., Gehrels, G., Irving, A.J., Chesley, J.T., Hanchar, J.M., 1999. Dating mantle metasomatism: U-Pb geochronology of zircons in cratonic mantle xenoliths from Montana and Tanzania. Int. Kimberlite Conf. 7 (1), 754–756. https://doi.org/10.29173/ikc2872.
Ruggles, C.E., Morgan, S., Reber, J.E., 2021. A multiple-pulse emplacement model for the Shonkin Sag laccolith, Montana, USA. J. Struct. Geol. 149. https://doi.org/10.1016/j.jsg.2021.104378.
Santosh, M., Yang, Q.-Y., Mohan, M.R., Tsunogae, T., Shaji, E., Stayanarayanan, M., 2014. Cryogenian alkaline magmatism in the Southern Granulite Terrane, India: petrology, geochemistry, zircon U–Pb ages and Lu–Hf isotopes. Lithos 208-209, 430–445. https://doi.org/10.1016/j.lithos.2014.09.016.
Saravanan, S., Ramasamy, R., 1995. Geochemistry and petrogenesis of shonkinite and associated alkaline rocks of Tiruppattur Carbonatite Complex, Tamil Nadu. J. Geol. Soc. India 46 (3), 235–243. https://doi.org/10.17491/jgsi/1995/460304.
Scarberry, K.C., Yakovlev, P.V., Schwartz, T.M., 2020. Mesozoic Magmatism in Montana: Montana Bureau of Mines and Geology Special Publication 122. Geology of Montana, 1. Geologic History. Available online, accessed 04.05.25: https://mbmg.mtech.edu/pdf/geologyvolume/Scarberry_MesozoicMagmatism.pdf.
Schmidt, R.G., 1978. Rocks and Mineral Resources of the Wolf Creek Area, Lewis and Clark and Cascade Counties, Montana, 1441. Geological Society of America Bulletin.
Shadenkov, Ye.M., Orlova, M.P., Borisov, A.B., 1990. Pyroxenite and shonkinite of the MalyyMurun pluton–Intrusive analogues of lamproite. Int. Geol. Rev. 32, 1. https://doi.org/10.1080/00206819009465755.
Sheriff, S.D., Gunderson, J.A., 1990. Age of the Adel Mountain volcanic field, west-central Montana. Isochron/West v. 56, 21–23. Available online, accessed 06.03.25:

https://geoinfo.nmt.edu/publications/periodicals/isochronwest/56/iw_v56_p21.pdf.
Shirey, S.B., Kamber, B.S., Whitehouse, M.J., Mueller, P.A., Basu, A.B., 2008. A review of the isotopic and trace element evidence for mantle and crustal processes in the Hadean and Archean: Implications for the onset of plate tectonic subduction. In: Condie, Kent C., Pease, Victoria (Eds.), When Did Plate Tectonics Begin on Planet Earth? Geological Society of America. https://doi.org/10.1130/2008.2440(01).
Sichel, S.E., Carlson, R.W., Esperança, S., Araújo, A.L.N., Valença, J.G., 1997. Preliminary isotopic study of the alkalic intrusive complexes along the Cabo Frio Lineament, RJ, Brazil. In: South-American Symposium on Isotope Geology-Brazil.
Simpson, B., Ubide, T., Spandler, C., 2025. Drivers of critical metal enrichment in peralkaline magmas recorded by clinopyroxene zoning. Commun. Earth Environ. 6 (89). https://doi.org/10.1038/s43247-025-02040-7.
Solomatova, N.V., Caracas, R., 2021. Buoyancy and Structure of Volatile-Rich Silicate Melts. J. Geophys. Res. 126 (2), e2020JB021045. https://doi.org/10.1029/2020JB021045.
Sørensen, H., 1974. The Alkaline Rocks. John Wiley & Sons Ltd., London, Sydney, & Toronto.
Sun, S.-s, McDonough, W.F., 1989. Chemical and isotopic systematics of oceanic basalts: implications for mantle composition and processes. Geol. Soc. Lond. Spec. Publ. 42, 313–345. https://doi.org/10.1144/GSL.SP.1989.042.01.19.
Tang, M., Lee, C.-T.A., Chen, K., Erdman, M., Costin, G., Jiang, H., 2019. Nb/Ta systematics in arc magma differentiation and the role of arclogites in continent formation. Nat. Commun. 10 (235). https://doi.org/10.1038/s41467-018-08198-3.
Tyrrell, G.W., 1978. Origin of Igneous Rocks. In: The Principles of PETROLOGY. Springer, Dordrecht, pp. 148–170. https://doi.org/10.1007/978-94-011-6026-1_8.
Ubide, T., Kamber, B.S., 2018. Volcanic crystals as time capsules of eruption history. Nat. Commun. 9, 326. https://doi.org/10.1038/s41467-017-02274-w.
Ubide, T., Mollo, S., Zhao, J., Nazzari, M., Scarlato, P., 2019. Sector-zoned clinopyroxene as a recorder of magma history, eruption triggers, and ascent rates. Geochim. Cosmochim. Acta 251, 265–283. https://doi.org/10.1016/j.gca.2019.02.021.
United States Geological Survey (USGS), 1952. Geologic Setting of the Mountain Pass Rare Earth Element Deposits, San Bernadino County, California, Open-File Report 52-110. https://doi.org/10.3133/ofr52110.
Upadhyay, D., 2008. Alkaline magmatism along the southeastern margin of the Indian shield: Implications for regional geodynamics and constraints on craton–Eastern Ghats Belt suturing. Precambrian Res. 162 (1–2), 59–69. https://doi.org/10.1016/j.precamres.2007.07.012.
Upadhyay, D., Raith, M.M., Mezger, K., Hammerschmidt, K., 2006. Mesoproterozoic rift-related alkaline magmatism at Elchuru, Prakasam Alkaline Province, SE India. Lithos v. 89(3-4, 447–477. https://doi.org/10.1016/j.lithos.2005.12.015.
Valença, J.G., 1980. Geology, Petrography and Petrogenesis of some Alkaline Igneous Complexes of Rio de Janeiro State, Brazil. Ph.D. thesis,. Ontario University.
Vermeesch, P., Pease, V., 2021. A genetic classification of the tholeiitic and calc-alkaline magma series. Geochem. Perspect. Lett. 19, 1–6. https://doi.org/10.7185/geochemlet.2125.
Verplanck, P.L., Mariano, A.N., Mariano Jr., A., 2016. Rare Earth element ore geology of carbonatites. In: Rare Earth and Critical Elements in Ore Deposits, 18. Society of Economic Geologists. https://doi.org/10.5382/Rev.18.01.
Vijaya Kumar, K., Ratnakar, J., 2001. Petrogenesis of the Ravipadu gabbro pluton, Prakasam province, Andhra Pradesh. Geol. Soc. India 57 (2), 113–140.
Vijaya Kumar, K., Ernst, W.G., Leelanadam, C., 2011. Opening and closing of a Mesoproterozoic Ocean along the SE margin of India: textural, cathodoluminescence and SHRIMP analyses of zircon. In: American Geophysical Union Fall Meeting, San Francisco, USA, (December 5th–9th).
Vuke, S.M., 2000. Geologic Map of the Great Falls South 30′ x 60′ Quadrangle. Montana Bureau of Mines & Geology, Central Montana.
Vuke, S.M., 2014. Preliminary Geologic Map of the Dearborn River 30′ x 60′ Quadrangle. Montana Bureau of Mines & Geology, West-Central Montana.
Wang, Z.-C., Zhou, M.-F., Li, M.Y.H., Robinson, P.T., Harlov, D.E., 2022. Kinetic controls on Sc distribution in diopside and geochemical behavior of Sc in magmatic systems. Geochim. Cosmochim. Acta 325, 316–332. https://doi.org/10.1016/j.gca.2022.03.016.
Wang, W., Lu, Y., Gao, L., Sun, G., Zhou, X., Yao, J., Yang, W., Liang, X., 2024. Late Archean K-rich intermediate magmatism driven by deep supracrustal recycling. Chem. Geol. 662. https://doi.org/10.1016/j.chemgeo.2024.122215.
Watts, K.E., Andersen, A.K., 2025. Complex carbonate ore mineralogy in the Mountain Pass carbonatite rare earth element deposit, USA. Am. Mineral. https://doi.org/10.2138/am-2025-9822.
Watts, K.E., Haxel, G.B., Miller, D.B., 2021. Temporal and petrogenic links between Mesoproterozoic alkaline and carbonatite magmas at Mountain Pass, California. Econ. Geol. 117 (1), 1–23. https://doi.org/10.5382/econgeo.4848.
Weed, W.H., Pirsson, L.V., 1895. Highwood mountains of Montana. J. Geol. 3, 851–853. https://www.jstor.org/stable/30055077.
Whisner, S.C., Schmidt, C.J., Whisner, J.B., 2014. Structural analysis of the Lombard thrust sheet and adjacent areas in the Helena salient, southwest Montana, USA. J. Struct. Geol. 69 (B), 351–376. https://doi.org/10.1016/j.jsg.2014.08.006.
Whiting, C.K., 1977. Small Laccoliths and Feeder Dikes of the Northern Adel Mountain Volcanics. University of Montana, Missoula unpub. Master's thesis. Available online, accesses 04.05.25. https://scholarworks.umt.edu/etd-geosciences/index.5.html.
Whitmeyer, S.J., Karlstrom, K.E., 2007. Tectonic model for the Proterozoic growth of North America. Geosphere 3, 220–259. https://doi.org/10.1130/GES00055.1.
Wilkinson, J.F.G., 1982. The genesis of mid-ocean ridge basalt. Earth Sci. Rev. 18 (1), 1–57. https://doi.org/10.1016/0012-8252(82)90002-2.
Wilson, M., 1989. Geochemical characteristics of igneous rocks as petrogenetic indicators. In: Igneous Petrogenesis. Springer, Dordrecht. https://doi.org/10.1007/978-94-010-9388-0_2.
Xia, L.-Q., 2014. The geochemical criteria to distinguish continental basalts from arc related ones. Earth-Sci. Rev. 139, 195–212. https://doi.org/10.1016/j.earscirev.2014.09.006.
Yaxley, G.M., Anenburg, M., Tappe, S., Decree, S., Guzmics, T., 2022. Carbonatites: classification, sources, evolution, and emplacement. Ann. Rev. Earth Planet. Sci. 50, 261–293. https://doi.org/10.1146/annurev-earth-032320-104243.
Zafar, T., Leng, C.-B., Zhang, X.-C., Rehman, H.U., 2019. Geochemical attributes of magmatic apatite in the Kukaazi granite from western Kunlun orogenic belt, NW China: implications for petrogenesis and Pb-Zn (-Cu-W) mineralization. J. Geochem. Explor. 204. https://doi.org/10.1016/j.gexplo.2019.06.005.
Zhang, X., Guo, F., Zhang, B., Zhao, L., Wu, Y., Wang, G., Alemayahu, M., 2020. Magmatic evolution and post-crystallization hydrothermal activity in the early Cretaceous Pingtan intrusive complex, SE China: records from apatite geochemistry. Contrib. Mineral. Petrol. 175 (35). https://link.springer.com/article/10.1007/s00410-020-1675-2.
Zhou, J.-S., Wang, Q., Xing, C.-M., Ma, L., Hao, L.-L., Li, Q.-W., Wang, Z.-L., Huang, T.-Y., 2021. Crystal growth of clinopyroxene in mafic alkaline magmas. Earth Planet. Sci. Lett. 568. https://doi.org/10.1016/j.epsl.2021.117005.